

Honours Thesis

*Author:*

Wilton Deany

*Supervisor:*

Prof. Peter Skands

June 30 2023

## **Abstract**

Modern collider phenomenology continues to transition towards precision tests of the standard model of particle physics. The Monte-Carlo event generators which underpin these studies are consequently being upgraded to meet the requirements of emerging high-energy experiments. In this thesis, we improve one such numerical code, the VINCIA parton-shower event generator. We first develop the all-orders formalism necessary to describe the complexity of parton-shower topologies, including a detailed implementation. Subsequently, we demonstrate the theorised shortcomings associated with hard, wide-angle gluon emission in the context of logarithmic accuracy. Finally, we propose a novel ‘jet-antenna’ kinematics scheme designed to overcome these deficiencies, and make comparisons to the existing dipole-antenna recoil map. With our initial model we observe an improvement across a significant portion of the phase space surveyed, and prepare for implementation in a fully-fledged shower algorithm.

# Contents

|          |  |           |
|----------|--|-----------|
| <b>1</b> | <b>An Introduction to Parton Shower Event Generators</b> | <b>1</b>  |
| 1.1      | Elements of Quantum Chromodynamics . . . . .             | 2         |
| 1.2      | Calculating Observables . . . . .                        | 3         |
| 1.3      | Factorisation and Universality . . . . .                 | 4         |
| 1.4      | Antenna Functions and Conventions . . . . .              | 6         |
| <b>2</b> | <b>A Simple Parton-Shower Algorithm</b>                  | <b>8</b>  |
| 2.1      | The Evolution Equation . . . . .                         | 8         |
| 2.2      | Running Coupling and Evolution Windows . . . . .         | 11        |
| 2.3      | Generating New Partons . . . . .                         | 12        |
| 2.4      | The Recoil Scheme . . . . .                              | 14        |
| <b>3</b> | <b>The Accuracy of the Vincia Antenna-Shower</b>         | <b>16</b> |
| 3.1      | Logarithmic Accuracy . . . . .                           | 16        |
| 3.2      | Attempting a Numerical Study . . . . .                   | 18        |
| <b>4</b> | <b>Novel Jet-Antenna Kinematics</b>                      | <b>20</b> |
| 4.1      | Motivating Jet Recoil . . . . .                          | 20        |
| 4.2      | The Jet-Antenna Kinematics Map . . . . .                 | 21        |
| 4.3      | Numerical Analysis . . . . .                             | 22        |
| 4.4      | Consensus and Future Extensions . . . . .                | 24        |
| <b>5</b> | <b>Conclusions</b>                                       | <b>26</b> |

Units and conventions.

This work will be carried out in natural units  $\hbar = 1 = c$ . All vectors and inner-products will use Lorentz four-vectors, with the the mostly-minus Minkowski signature, unless otherwise made clear by **bold-face** symbols.

Acknowledgements.

I thank my supervisor, Peter Skands, for the two incredible years he has spent teaching me theoretical physics. His ability to explain difficult concepts in simple terms was indispensable. I also thank Christian Preuss, Stefan Höche and Javira Altmann for their contributions to this work. I thank Paul Lasky and my fellow honours students for their guidance and banter. Finally, I give special thanks to Ellie Mead, Imogen Stephenson, Niamh Corbett, William Searle, Russel Demos and Clare Olding for the morale I needed to see this thesis through.

# 1 An Introduction to Parton Shower Event Generators

The energy scales accessible by modern particle colliders can achieve energies up to order 10 TeV, which correspond to interactions on a length scale of  $10^{-18}\text{m}$  [1]. If an experimentalist wanted to directly observe the production and decay of a fundamental particle at this length scale, they would consequently need an impossibly small detector. Naturally they instead resort to *indirect* observation, whereby they attempt to detect the *products* of the process they are interested in. Such products will typically be an assortment of leptons, mesons, and baryons, which will be intercepted and analysed by the apparati at a macroscopic scale.

These indirect observations have motivated the development of general-purpose Monte-Carlo event generators (MCEGs). Such programs are ubiquitous in modern collider-physics since they enable the simulation the high-energy dynamics not directly measurable by detectors. MCEGs facilitate this capability by providing a map from the fundamental process of interest, the initial state  $|i\rangle$ , to the experimental detection, the final state  $|f\rangle$ . They thus describe the intermediate evolution which is inaccessible to the detector. There exists a variety of MCEGs, each with a unique formalism for this evolution. They are ‘general-purpose’, in the sense that they are designed to calculate, at least approximately, the majority of observables that we could wish to study, with a single underlying model. They do this with stochastic ‘Monte-Carlo’ methods, which iteratively *generate* a given collider *event*.

Fully fledged event generators typically simulate the event with two consecutive models; a ‘parton-shower’ model, followed by a ‘hadronisation’ model. The former describes the bremsstrahlung cascade (shower) of intense, approximately collimated radiation which follows the initial process we are interested in. The latter describes the process by which much of this newly emitted brehmstrallung will stabilise into bound states; the hadrons detected by the apparati. The hadronisation process produces the final state  $|f\rangle$ , which is what the detector measures. The parton shower is the intermediate model which *maps* the initial state  $|i\rangle$  to the pre-hadronisation ‘final’ state  $|h\rangle$ . The hadronisation model then takes over and maps  $|h\rangle \rightarrow |f\rangle$ .

This work will focus primarily on parton-shower models, making reference to hadronisation models [2–5] only when relevant to the broader context.

Historically, multiple event generators have facilitated the development of modern particle physics. The numerical codes PYTHIA [6], HERWIG [7] and SHERPA [8] are particularly ubiquitous. A number of smaller-in-scope generator models have also been instrumental, with a long history of meta-studies and prototype formalisms, cementing event-generation as a sub-field of study in its own right.

Of particular interest to this work is one such contemporary shower model, the VINCIA formalism [9, 10]. The Vincia event generator is based on the Pythia formalism. Most of the following work will describe methods and results from Vincia, referring to other relevant formalisms where relevant. Namely, the ALARIC [11], ARIADNE [12], DIRE [13], and PanScales [14] event generators.

This work will begin with an introduction to parton shower models in general, including a specific discussion of the Vincia parton-shower formalism. Within section 2 we will discuss the application of this formalism in an explicit parton-shower algorithm. These sections are intended to describe all aspects of the formalism needed to assess the logarithmic-accuracy of Vincia. Section 3 is dedicated to the discussion of some known issues with existing parton-showers in the same family as Vincia. This relies upon the framework of logarithmic resummation, and represents ongoing development. Finally, section 4 introduces the initial implementation of a novel kinematics map partially designed to rectify some of the aforementioned shortcomings.

## 1.1 Elements of Quantum Chromodynamics

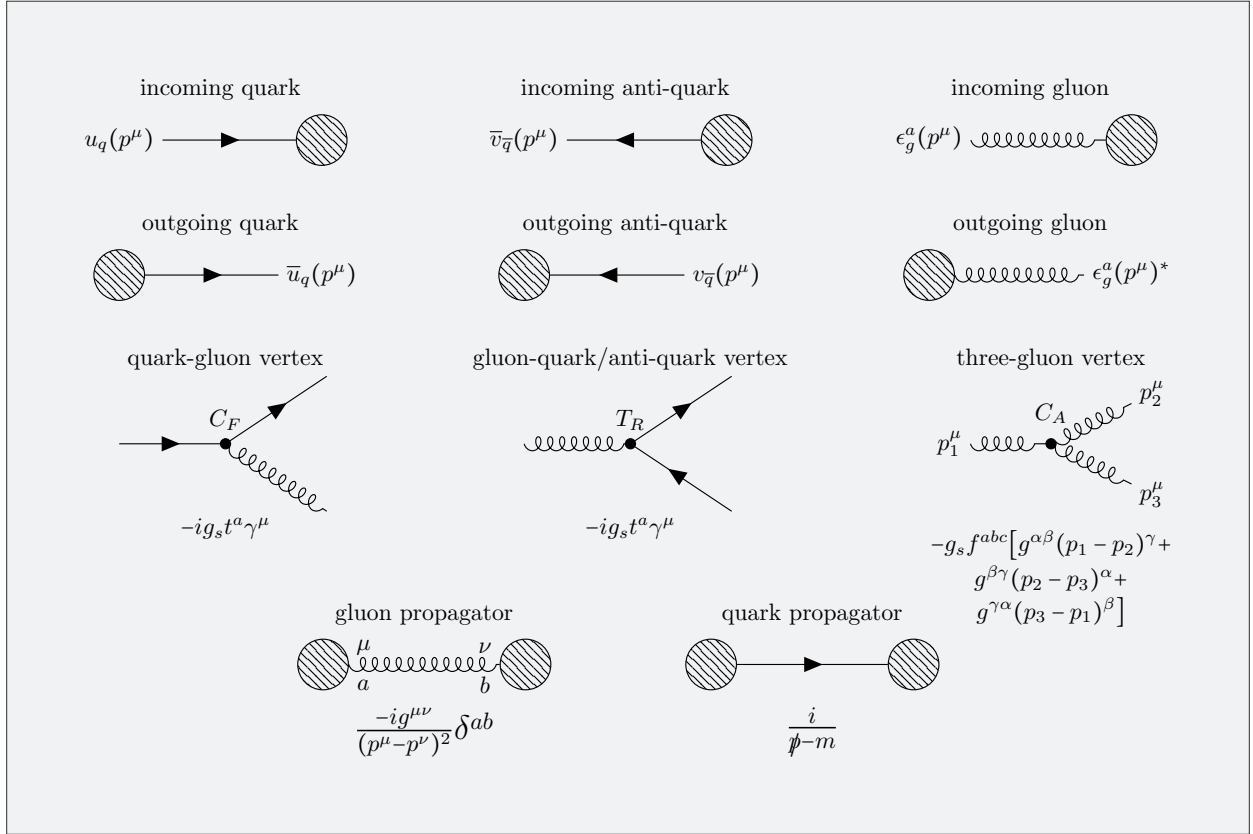


Figure 1: Relevant Feynman rules for QCD. Vertex factors for the three possible processes are given, with the associated colour factors (Casimirs),  $C_A$ ,  $C_F$  and  $T_R$ . Greek indices are reserved for four-vectors while Latin indices  $a, b, c = \{1, \dots, 8\}$  denote colour combinations.

Parton-shower event generators primarily model the dynamics of hadronic interactions. This capability enables the study of the subatomic constituents, quarks and gluons, collectively dubbed ‘partons’. In the context of MCEGs, partons are described within the framework of perturbative quantum field theory (pQFT). Specifically, the behaviour of partons is modelled by the theory of quantum chromodynamics (QCD); an  $SU(3)$  gauge theory. QCD is similar to its electromagnetic counterpart, quantum electrodynamics (QED), with which this work assumes some familiarity. However, there remains a number of distinguishing features, made apparent by the associated QCD Lagrangian

$$\mathcal{L}_{\text{QCD}} = \underbrace{\sum_q \bar{\psi}_q^i (i\gamma^\mu (D_\mu)_{ij} - m_q \delta_{ij}) \psi_{qj}}_{\text{QCD Dirac Lagrangian}} - \frac{1}{4} F_{\mu\nu}^a F^{a\mu\nu}, \quad (1.1)$$

$$\psi_q^i = \begin{pmatrix} \psi_q^{\text{red}} \\ \psi_q^{\text{green}} \\ \psi_q^{\text{blue}} \end{pmatrix}, \quad (D_\mu)_{ij} = \partial_\mu \delta_{ij} - ig_s t_{ij}^a G_\mu^a, \quad F_{\mu\nu}^a = \partial_\mu G_\nu^a - \partial_\nu G_\mu^a + \underbrace{g_s f^{abc} G_\mu^b G_\nu^c}_{\text{non-Abelian term}}, \quad (1.2)$$

where  $q$  runs over the six quark flavours. This Lagrangian has the same overall structure as the  $U(1)$  QED Lagrangian, including a QCD-analogue of the Maxwell equations. However unlike the single electric charge of the  $U(1)$  theory, the  $SU(3)$  structure of QCD endows it with three ‘colour charges’, {red, green, blue}, indexed by the three-component spinor  $\psi_q^i$ . The anti-spinor  $\bar{\psi}_q^i$  is likewise associated with the anti-colour charges {cyan, magenta, yellow}.

The gluons live in the adjoint representation and consequently have eight components, often represented as combinations of colour and anti-colour. These components are tracked by  $a = \{1, \dots, 8\}$  and assigned to the gluon field  $G^a$ , the Gell-Mann generators  $t^a$ , and the structure constants  $f^{abc}$  which are beyond the scope of this work [15].

The factor  $g_s$  gives the coupling strength between the quark spinor-field and the gluon vector-field, analogous to  $e$  in QED. However the non-Abelian term in the gluon field-strength tensor  $F_{\mu\nu}^a$  allows for the gluon field to couple to itself, with strength  $g_s$ . Owing to the structure of U(1), this is not a feature of QED, where the analogous boson, the photon, cannot interact with itself. Consequently, a gluon can radiate gluons.

## 1.2 Calculating Observables

In the context of collider experiments, the quantity of interest is typically a differential cross-section  $d\sigma$  measured with respect to some observable  $\mathcal{O}$ . This is just a measure of the normalised ‘amount’ of that observable per  $d\mathcal{O}$ . Perturbative quantum field theory provides the framework to calculate the differential cross-section

$$\frac{d\sigma}{d\mathcal{O}} = \int d\Phi |\mathcal{M}|^2 \delta(\mathcal{O} - \mathcal{O}(\{p\}_\Phi)). \tag{1.3}$$

The integral is over  $d\Phi$ , the Lorentz-invariant phase-space measure. The associated  $\delta$ -function ensures momentum-conservation for the set of momenta  $\{p\}$  in the phase-space  $\Phi$ . The squared matrix-element  $|\mathcal{M}|^2$  contains the information about the possible QCD interactions. For our purposes,  $\mathcal{M}$  describes the transition from the initial state  $|i\rangle$  to the final hadronisation state  $|h\rangle$ . Simple matrix-elements may be calculated with the associated QCD Feynman-rules presented in Fig. 1. However, the complexity of modern high-energy topologies renders Feynman diagram calculations for such events intractable. This intractability is the problem which MCEGs are intended to circumvent.

This may be understood by considering a high-energy interaction which produces two quarks, a state which we label  $X$ . There are an infinite number of Feynman diagrams which contribute to this process, which may be conveniently depicted as a superposition of states with the  $\langle$ bra|ket $\rangle$  notation,

$$\mathcal{M}_X = \underbrace{\left[ \dots \right]}_{\mathcal{M}_X^{(0)} \text{ (LO)}} + \underbrace{\left[ \dots \right]}_{\mathcal{M}_X^{(1)} \text{ (NLO)}} + \dots + \underbrace{\left[ \dots \right]}_{\mathcal{M}_X^{(2)} \text{ (NNLO)}} + \dots + \underbrace{\left[ \dots \right]}_{\mathcal{M}_X^{(n)} \text{ (N}^n\text{LO)}} + \dots \tag{1.4}$$

The above notation allows us to track the order in perturbation theory of each contributing matrix-element. The leading-order (LO) term  $\mathcal{M}_X^{(0)}$  is often called the Born-level contribution. Subsequent contributions represent virtual-corrections to the Born-level, labelled next-to-leading-order (NLO) and so forth. The number of additional virtual particles is denoted by the superscript  $(n)$ . The QCD Feynman-rules dictate that each newly emitted particle is associated with a vertex factor, containing a factor of  $g_s$ . Hence, the Born-level process contains one factor of  $g_s$ , while the NLO process has three factors of  $g_s$ , and so-on.

Eq. (1.3) requires the squared the matrix-element  $|\mathcal{M}_X|^2$ . We calculate the first few

terms:

$$\begin{aligned}
 |\mathcal{M}_X|^2 &= \mathcal{M}_X^\dagger \mathcal{M}_X = |\mathcal{M}_X^{(0)}|^2 + 2\text{Re} \left[ (\mathcal{M}_X^{(0)})^\dagger (\mathcal{M}_X^{(1)}) \right] + |\mathcal{M}_X^{(1)}|^2 + \dots \\
 &= \underbrace{\left\langle \text{---} \circ \text{---} \right\rangle}_{\mathcal{O}(\alpha_s)} + 2\text{Re} \left\langle \text{---} \circ \text{---} \right\rangle_{\mathcal{O}(\alpha_s^2)} + \underbrace{\left\langle \text{---} \circ \text{---} \right\rangle}_{\mathcal{O}(\alpha_s^3)} + \dots
 \end{aligned} \tag{1.5}$$

where  $\alpha_s = g_s^2/4\pi$  is the strong coupling constant. The three inner-products presented above have two, four, and six factors of  $g_s$  respectively, and are thus of order one, two and three in  $\alpha_s$  respectively. Provided  $\alpha_s$  is small, the series may be truncated at a user defined order in  $\alpha_s$ . Nevertheless, a truly general-purpose parton-shower model must provide an approximate all-orders description of the evolution. The following sections are dedicated to this requirement.

It is important to note that  $\alpha_s$  is not constant, but in-fact depends on the energy scale  $Q^2$  of the process in question [16]. This ‘running’ of the strong coupling will be explored in section 2.2, but for brevity, lower scales correspond to higher values of  $\alpha_s(Q^2)$ . Below scales of approximately  $\Lambda_{\text{QCD}} = 1 \text{ GeV}$ , the aforementioned perturbative series will not suffice to describe the behaviour of QCD. Since the parton-shower is a strictly perturbative model, it is thus necessary to transition to non-perturbative hadronisation models below this scale.

### 1.3 Factorisation and Universality

The Lagrangian for QCD presented in Eq. (1.2) is approximately scale invariant, under transformations of the form  $x^\mu \rightarrow \lambda x^\mu$  [17]. This symmetry is broken by the running of  $\alpha_s$ , but at high-energy scales, asymptotic freedom allows for weakly-interacting quark and gluon fields [18, 19]. Such scale-invariance manifests itself in the structure of QCD matrix-elements, which contain ‘universal’ singularities, regardless of the order in perturbation theory [20]. This structure is referred to as ‘universality’. Since these divergent regions of phase space provide the dominant evolution of the shower, the way to proceed is as follows.

- Calculate the ‘radiation function’ corresponding to the dominant probability that the parton shower transitions from an  $n$ -parton state to an  $n + 1$ -parton state, via the emission of brehmstrahlung.
- Then, universality guarantees this radiation function will apply at all orders of  $\alpha_s$ , and can hence be used to iteratively generate radiative corrections to arbitrary topologies.
- Modify this radiation function for the specific emission being considered, and attempt to correct for any finite terms not accounted for by the singularity structure.
- Ensure that this description remains unitary, and conserve overall momentum by allowing parton momenta to vary appropriately as new emissions are included.

Following these guiding principles, we thus begin with a brief derivation of the desired radiation functions. Such functions vary between parton-shower formalisms, with the Vincia architecture explicitly designed for ‘dipole-antenna’ functions. These antenna functions describe the probability for two colour-connected partons to emit a third parton in a  $2 \rightarrow 3$

‘dipole’ process. The intention is thus to generate an  $n$ -parton topology by sequentially performing  $2 \rightarrow 3$  emissions, where one of the existing dipoles will be selected to radiate. The antenna functions may be derived following the example of [21]. We begin by writing the full, all-orders expansion to the cross section in Eq. (1.3),

$$\begin{aligned} \left. \frac{d\sigma}{d\mathcal{O}} \right|_{\mathcal{S}} &= \int d\Phi_X \left[ |\mathcal{M}_X^{(0)}|^2 + 2\text{Re}[\mathcal{M}_X^{(0)\dagger} \mathcal{M}_X^{(0)}] \right] \delta(\mathcal{O} - \mathcal{O}(\{p\}_X)) \\ &+ \int d\Phi_{X+1} |\mathcal{M}_{X+1}^{(0)}|^2 \delta(\mathcal{O} - \mathcal{O}(\{p\}_{X+1})) + \mathcal{O}(\alpha_s^3). \end{aligned} \quad (1.6)$$

For brevity only the NLO (order  $\alpha_s$  and  $\alpha_s^2$ ) terms are explicitly written. The matrix element  $\mathcal{M}_{X+k}^{(\ell)}$  denotes  $k$  radiative corrections (real emissions of new particles) to the Born-level process and  $\ell$  virtual corrections (internal loops).  $\mathcal{S}$  denotes the final topology after the parton shower has concluded, described by the final-state momenta  $\{p\}$ . Each term in the series only contains a subset of this total phase space, such as  $\{p\}_X$ , denoting the momenta in the Born level, and so-forth. The  $\delta$ -functions ensure that the integrals are only carried out over the phase-space relevant to each process.

We proceed by factoring out the Born-level term  $d\Phi_X |\mathcal{M}_X^{(0)}|^2$ ,

$$\begin{aligned} \left. \frac{d\sigma}{d\mathcal{O}} \right|_{\mathcal{S}} &= \int d\Phi_X |\mathcal{M}_X^{(0)}|^2 \left[ \left( 1 + \frac{2\text{Re}[\mathcal{M}_X^{(0)\dagger} \mathcal{M}_X^{(1)}]}{|\mathcal{M}_X^{(0)}|^2} \right) \delta(\mathcal{O} - \mathcal{O}(\{p\}_X)) \right. \\ &\left. + \int \frac{d\Phi_{X+1} |\mathcal{M}_{X+1}^{(0)}|^2}{d\Phi_X |\mathcal{M}_X^{(0)}|^2} \delta(\mathcal{O} - \mathcal{O}(\{p\}_{X+1})) + \mathcal{O}(\alpha_s^3) \right]. \end{aligned} \quad (1.7)$$

The above formulation of the cross section is an example of ‘factorisation’, where expression now consists of matrix-element ratios. It’s these ratios which contain the universal singular-structure we intend to harness.

The term in the square brackets is dubbed the ‘shower operator’,  $\hat{\mathcal{S}}$ . It will be responsible for the evolution from the Born-level state to an arbitrarily complex  $n$ -parton final state. To proceed, the KLN theorem [22, 23] may be invoked to replace the dependence on virtual corrections  $\mathcal{M}_X^{(\ell)}$  with integrals over the corresponding radiative correction  $\mathcal{M}_{X+k}^{(0)}$ . In doing so we ensure unitarity, since the divergence in one matrix-element ratio is now suppressed by the other. We have also implicitly removed the finite, non-divergent terms which must be restored a-posteriori [24, 25]. This allows the shower operator to be written as

$$\begin{aligned} \hat{\mathcal{S}} &= \left( 1 - \int \frac{d\Phi_{X+1} |\mathcal{M}_{X+1}^{(0)}|^2}{d\Phi_X |\mathcal{M}_X^{(0)}|^2} \right) \delta(\mathcal{O} - \mathcal{O}(\{p\}_X)) \\ &+ \int \frac{d\Phi_{X+1} |\mathcal{M}_{X+1}^{(0)}|^2}{d\Phi_X |\mathcal{M}_X^{(0)}|^2} \delta(\mathcal{O} - \mathcal{O}(\{p\}_{X+1})) + \mathcal{O}(\alpha_s^3). \end{aligned} \quad (1.8)$$

Next, we seek to cast this operator as a recursive Markov chain. We define the scales  $Q_{\text{start}}^2$  and  $Q_{\text{stop}}^2$  to be the initial and final scales of this chain, and define  $Q_{\text{emit}}^2$  to be the intermediate scale at which dipole emission occurs. Then the shower operator may be written recursively in the following form [26]

$$\begin{aligned} \hat{\mathcal{S}}(\{p\}_n, Q_{\text{start}}^2, Q_{\text{stop}}^2) &= \Delta(\{p\}_X, Q_{\text{start}}^2, Q_{\text{stop}}^2) \delta(\mathcal{O} - \mathcal{O}(\{p\}_X)) \\ &+ \int_{Q_{\text{start}}^2}^{Q_{\text{stop}}^2} \frac{d\Phi_{X+1} |\mathcal{M}_{X+1}^{(0)}|^2}{d\Phi_X |\mathcal{M}_X^{(0)}|^2} \Delta(\{p\}_X, Q_{\text{start}}^2, Q_{\text{emit}}^2) \hat{\mathcal{S}}(\{p\}_{X+1}, Q_{\text{emit}}^2, Q_{\text{stop}}^2). \end{aligned} \quad (1.9)$$

Subsequently, we introduce the Sudakov factor  $\Delta$  to maintain unitarity [27]. It is derived in the manner of traditional nuclear decay models, by requiring that the second line of the shower operator be equal to the negative derivative of the first,

$$\Delta(\{p\}_n, Q_1^2, Q_2^2) = \exp \left[ - \int_{Q_1^2}^{Q_2^2} \frac{d\Phi_{X+1}}{d\Phi_X} \frac{|\mathcal{M}_{X+1}^{(0)}|^2}{|\mathcal{M}_X^{(0)}|^2} \right]. \quad (1.10)$$

The Sudakov factor describes the probability of no evolution between two scales  $Q_1^2$  and  $Q_2^2$ . Hence the first term of Eq. (1.9) gives the probability of no emission, while the second term gives the probability of at-least one emission. The nested recursion of the Sudakov factor restarts from the scale  $Q_{\text{emit}}^2$ , allowing for subsequent emissions below this scale. Note that we have implicitly imposed an ordering on the scale  $Q^2$ . Taking  $Q_{\text{start}}^2 > Q_{\text{stop}}^2$ , we consequently require that each successive emission occur at a lower scale than the previous.

## 1.4 Antenna Functions and Conventions

The next task is to derive the dipole-antenna functions explicitly. There are many such functions, each with variations in the singular structure depending on the context. Here we will focus on deriving the universal singular structure and defer the reader to more detailed descriptions [28].

The advantage of the dipole-antenna formalism is that the fully-coherent radiation pattern of a colour dipole is manifest. This is demonstrated with Feynman rules by considering the full contribution to the matrix-element ratio in Eq. (1.10)

$$\frac{|\mathcal{M}_{X+1}^{(0)}|^2}{|\mathcal{M}_X^{(0)}|^2} = \left[ \left\langle \begin{array}{c} \text{---} \text{---} \\ \text{---} \text{---} \end{array} \right\rangle + 2\text{Re} \left\langle \begin{array}{c} \text{---} \text{---} \\ \text{---} \text{---} \end{array} \right\rangle + \left\langle \begin{array}{c} \text{---} \text{---} \\ \text{---} \text{---} \end{array} \right\rangle \right] \div \left\langle \begin{array}{c} \text{---} \text{---} \\ \text{---} \text{---} \end{array} \right\rangle. \quad (1.11)$$

Note that the numerator sums over all combinations, including the interference term in the middle. There are standard textbook procedures for carrying out such calculations [29]. With this in mind, we discuss this in the notation best suited to the Vincia shower, introduced in [30], which will be used henceforth.

Universality ensures Eq. (1.11) will generalise to arbitrary  $2 \rightarrow 3$  processes. We thus assign the labels  $I$  and  $K$  to the two partons in the denominator process  $|\mathcal{M}_2^{(0)}|$ . These are the pre-branching partons, or ‘parents’, for which we reserve capital letters in their labelling. In the Numerator  $\mathcal{M}_3^{(0)}$ , there are three partons, for which we use lower-case labelling,  $i, j, k$ . These are the post-branching or ‘daughter’ partons. Partons  $i$  and  $k$  are inherited from  $I$  and  $K$  respectively, while  $j$  is reserved for the newly emitted parton.

With this notation the matrix-element ratio for gluon emission can be calculated as

$$\frac{|\mathcal{M}_3^{(0)}(p_i, p_j, p_k)|^2}{|\mathcal{M}_2^{(0)}(p_I, p_K)|^2} = \left| g_s \sum_{\lambda=1,2} \sum_{a=1}^8 t^a \left( \frac{(p_k)^\mu (\epsilon_a^\lambda)_\mu}{(p_k)^\nu (p_j)_\nu} - \frac{(p_i)^\mu (\epsilon_a^\lambda)_\mu}{(p_i)^\nu (p_j)_\nu} \right) \right|^2. \quad (1.12)$$

Here,  $p_i, p_j, p_k$  are the four-momenta of those respective partons, and  $\epsilon_a^\lambda$  are the gluon polarisation vectors. For intuitive purposes, we derived this result by implicitly assuming parton- $j$  was ‘soft’, meaning  $p_j \ll \{p_I, p_K\}$ , though the basic result will hold in general. We assume unpolarised gluons, thus averaging over the states, and introduce the following useful notation.

We write the Lorentz-invariant inner-product between two four-vectors:  $p_1^\mu, p_2^\mu$ , as  $s_{12} = 2p_1^\mu p_{2\mu}$ . This produces the following useful relation

$$m_{IK}^2 = (p_I^\mu + p_K^\mu)^2 = s_{IK} + m_I^2 + m_K^2 = s_{ij} + s_{jk} + s_{ik} + m_i^2 + m_j^2 + m_k^2. \quad (1.13)$$

We can use this notation in Eq. (1.12) to carry out the average over the initial states and sum over the final states. This leads to the following central result

$$\frac{|\mathcal{M}_3^{(0)}(p_i, p_j, p_k)|^2}{|\mathcal{M}_2^{(0)}(p_I, p_K)|^2} = g_s^2 \mathcal{C}_{ijk} \left[ \frac{2s_{ik}}{s_{ij}s_{jk}} - \frac{2m_I^2}{s_{ij}^2} - \frac{2m_K^2}{s_{jk}^2} \right] \xrightarrow{\text{massless}} g_s^2 \mathcal{C}_{ijk} \left[ \frac{2s_{ik}}{s_{ij}s_{jk}} \right], \quad (1.14)$$

where  $\mathcal{C}_{ijk}$  is a normalisation constant containing the colour-Casimirs and other factors. Particularly in the massless case, this function is referred to as the ‘soft-eikonal’ radiation function. Although generally difficult to prove [20], the soft-eikonal function is universal to all QCD processes involving the ratio between matrix elements. In the context of the Vincia parton-shower, the class of radiation functions to which the soft-eikonal term belongs are collectively known as ‘antenna functions’.

In the convention of [26, 28] the antenna-functions of concern to this work are written as

$$\begin{aligned} a^0(s_{ij}, s_{jk}, s_{ik}) &= \frac{g_s^2 \mathcal{C}_{ijk}}{\sqrt{\lambda(s_{IK}, m_I^2, m_K^2)}} \bar{a}^0(s_{ij}, s_{jk}, s_{ik}) \\ &= \frac{g_s^2 \mathcal{C}_{ijk}}{\sqrt{\lambda(s_{IK}, m_I^2, m_K^2)}} \left[ \frac{2s_{ik}}{s_{ij}s_{jk}} - \frac{2m_I^2}{s_{ij}^2} - \frac{2m_K^2}{s_{jk}^2} + \text{subleading terms} \right], \end{aligned} \quad (1.15)$$

which is normalised by the Källén function  $\lambda(s_{IK}, m_I^2, m_K^2) = s_{IK}^2 + m_I^4 + m_K^4 - 2s_{IK}m_I^2 - 2s_{IK}m_K^2 - 2m_I^2m_K^2$ . The function  $\bar{a}^0$  in the square-brackets is the ‘colour-coupling stripped’ antenna-function, containing only the masses and invariants. In general there will be other subleading terms in the antenna function, but the soft-eikonal will be the dominant. To see this we can introduce a frame dependant, but useful representation of the invariants

$$s_{ij} = 2E_i E_j (1 - \cos \theta_{ij}) \quad s_{jk} = 2E_j E_k (1 - \cos \theta_{jk}). \quad (1.16)$$

These terms will separately go to zero in the ‘collinear’ limit, where the angle of parton  $j$  is zero with respect to either  $i$  or  $k$ . Similarly both terms will go to zero simultaneously in the ‘soft’ limit, where the energy of parton  $j$  is zero. The soft and collinear scenarios both correspond to divergences of the antenna function, representing the singular regions of phase space where the probability of emission is enhanced. The denominator of Eq. (1.14) thus contains a double singularity in the soft limit, and this soft-eikonal term thus meets our criteria for a dominant radiation function. The subleading terms will also each contribute a single additional divergence, making them subdominant. An advantage of the dipole-antenna functions is that they manifestly describe both the soft and collinear limits. For example, the early and prominent DGLAP formalism leverages the collinear limits of individual partons only, limiting it to  $1 \rightarrow 2$  processes. This neglects the soft-eikonal structure of soft  $2 \rightarrow 3$  emission from colour dipole, which must instead be reinstated a-posteriori [31–33].

We have thus derived our dominant and universal radiation function. We will not discuss the available methods for improving such antenna functions, as the soft-eikonal term will suffice in this work. From this, we can now construct a simple shower algorithm from the above components.

## 2 A Simple Parton-Shower Algorithm

Having introduced the theoretical structure of the parton shower algorithm, we devote this section to a detailed description of the Vincia dipole-antenna shower. This is intended to clarify elements of the algorithm which are not explicitly described in the literature. This is necessary for reproducibility, and to highlight all aspects of algorithm which may be susceptible to numerical instability, which will be relevant in section 3.2.

We will not describe all elements of the algorithm in full, but each of the important components will be present. Any additional details should thus be accessible in the official documentation, and transparent given the context provided within this section. We emphasise that we will only consider  $q \rightarrow qg$  and  $g \rightarrow gg$  vertices, while  $g \rightarrow q\bar{q}$  and all QED effects will be omitted. We present the algorithm in the context of a  $Z^0$ -decay, implying an initial center-of-mass energy of  $m_Z^2 = 91.188^2 \text{ GeV}^2$ .

### 2.1 The Evolution Equation

Our first task is to re-write the Sudakov factor, Eq. (1.10) in a more approachable form. To do this, we choose the scales  $Q_i^2$  and  $Q_j^2$ . Vincia belongs to a class of showers which order their emissions with respect to the transverse momenta  $p_\perp$  of the radiative corrections. Such  $p_\perp$ -ordered showers start from the hardest (large  $p_\perp$ ) emission and produce progressively softer (small  $p_\perp$ ) emissions. Vincia uses the Ariadne definition [12] of transverse momentum, given by the shower invariants

$$p_\perp^2 = \frac{s_{ij}s_{jk}}{s_{IK}} \quad \Rightarrow \quad x_\perp = \frac{p_\perp^2}{s_{IK}} = y_{ij}y_{jk} \quad (2.1)$$

where  $x_\perp$  is the convenient dimensionless equivalent, using  $y_{ij} = s_{ij}/s_{IK}$  and  $y_{jk} = s_{jk}/s_{IK}$ .

The transverse-momentum squared  $p_\perp^2$  becomes the ‘evolution variable’, and we make the replacement  $Q^2 \rightarrow p_\perp^2$ . The Sudakov factor can then be expressed as

$$\begin{aligned} \Delta_{IK \rightarrow ijk}(p_{\perp 1}^2, p_{\perp 2}^2) &= \exp\left(-\mathcal{A}_{IK \rightarrow ijk}(p_{\perp 1}^2, p_{\perp 2}^2)\right) \\ &= \exp\left(-\int_{p_{\perp 1}^2}^{p_{\perp 2}^2} \frac{d\Phi_3^{ijk}}{d\Phi_2^{IK}} a_{IK \rightarrow ijk}^0(s_{ij}, s_{jk}, s_{IK})\right). \end{aligned} \quad (2.2)$$

This expression represents the probability that a state  $|IK\rangle$  at scale  $p_{\perp 1}^2$  will transition to a state  $|ijk\rangle$  at scale  $p_{\perp 2}^2$ . Vincia samples randomly from this distribution by setting  $\Delta = R \sim \mathcal{U}(0, 1)$ , and solving Eq. (2.2) for  $p_{\perp 2}^2$ . Assuming the starting scale  $p_{\perp 1}^2$  is known, this procedure gives the following equation to be solved.

$$R = \exp\left[-\mathcal{A}_{IK \rightarrow ijk}(p_{\perp 1}^2, p_{\perp 2}^2)\right] \quad (2.3)$$

However, the integral in the exponent is typically too cumbersome to work with directly. This can be overcome by introducing a trial antenna-function, which is an overestimate to the real antenna function,

$$\bar{a}_{\text{trial}}^0 \geq \bar{a}_{IK \rightarrow ijk}^0. \quad (2.4)$$

We can then use a Monte-Carlo accept-reject procedure to recover the correct distribution, the details of which we defer to section 2.3. The simplest and canonical [34] choice for this

trial function is the most singular term of the soft-eikonal antenna-function,

$$\bar{a}_{\text{trial}}^0(s_{ij}, s_{jk}, s_{IK}) = \frac{2s_{IK}^2}{s_{ij}s_{jk}}. \quad (2.5)$$

The other component needed for Eq. (2.2) is the phase-space ratio  $d\Phi_3^{ijk}/d\Phi_2^{IK}$  which can be derived [3] from the ratio between phase-space factors  $d\Phi_3^{ijk}$  and  $d\Phi_2^{IK}$  for three and two parton interactions respectively. Stating the result in terms of the Källén function [9] produces

$$\frac{d\Phi_3^{ijk}}{d\Phi_2^{IK}} = \frac{1}{16\pi^2} \frac{ds_{ij}ds_{jk}}{\sqrt{\lambda(s_{IK}, m_I^2, m_K^2)}} \frac{d\phi}{2\pi}. \quad (2.6)$$

This expression is simplified by assuming unpolarised partons, allowing  $d\phi/2\pi$  to be integrated away. Eq. (2.2) may now be written with this phase-space ratio and the trial antenna-function,

$$\begin{aligned} \mathcal{A}_{IK \rightarrow ijk}(p_{11}^2, p_{12}^2) &= \int_{p_{11}^2}^{p_{12}^2} \frac{d\Phi_3^{ijk}}{d\Phi_2^{IK}} \frac{4\pi\mathcal{C}\alpha_s(p_{\perp}^2)}{\sqrt{\lambda(s_{IK}, m_I^2, m_K^2)}} \bar{a}_{\text{trial}}^0(s_{IK}, s_{ij}, s_{jk}) \\ &= \frac{f_{\lambda}^2}{2\pi} \mathcal{C} \int_{p_{11}^2}^{p_{12}^2} \alpha_s(p_{\perp}^2) \frac{ds_{ij}ds_{jk}}{s_{ij}s_{jk}}, \end{aligned} \quad (2.7)$$

where the  $p_{\perp}^2$  scale dependence of  $\alpha_s$  necessitates that it stay in the integrand for now. We have also ‘dressed’ the stripped-antenna function  $\bar{a}_{\text{trial}}^0$  with the appropriate colour-coupling factors using Eq. (1.15). Finally, we introduced the Källén function for convenience,

$$f_{\lambda} = \frac{s_{IK}}{\sqrt{\lambda(s_{IK}, m_I^2, m_K^2)}} \xrightarrow{\text{massless}} 1. \quad (2.8)$$

We would now like to change variables in order to integrate over  $p_{\perp}^2$  instead of  $s_{ij}, s_{jk}$ . We do this with dimensionless quantities for convenience by introducing a second phase-space variable,

$$y = \frac{1}{2} \ln \left( \frac{s_{jk}}{s_{ij}} \right), \quad (2.9)$$

which we interpret as a pseudorapidity to accompany  $x_{\perp}$ . With the transformation of variables  $s_{ij} = s_{IK}e^{-y}\sqrt{x_{\perp}}$  and  $s_{jk} = s_{IK}e^y\sqrt{x_{\perp}}$ , we can re-express Eq. (2.7) in the simplified form,

$$\mathcal{A}_{IK \rightarrow ijk}(x_{11}, x_{12}) = f_{\lambda} \frac{\mathcal{C}}{2\pi} \int_{x_{11}}^{x_{12}} \int_{y_{-}(x_{\perp})}^{y_{+}(x_{\perp})} \alpha_s(x_{\perp}) d\ln x_{\perp} dy, \quad (2.10)$$

where  $y_{+}(x_{\perp}), y_{-}(x_{\perp})$  are the  $x_{\perp}$ -dependant rapidity bounds. The  $x_{\perp}$  dependence of  $\alpha_s$  complicates the integral, but for now we can take a constant value of  $\alpha_s$  and recover the physical value with a veto similar to the physical-rapidity veto introduced in section 2.3. We then impose a running coupling, described in the next section.

With this  $\alpha_s$ , our choice of variables imply flat contours in the  $\ln x_{\perp}$ - $y$  phase space, since the above integrand is now constant for  $\bar{a}_{\text{trial}}^0$ . We can use this description to visualise the phase-space evolution with ‘Lund-diagrams’, depicted in Fig. 2. [35].

The phase-space planes for each dipole in the Lund-plane are referred to as ‘leaves’, with The rapidity interval in Eq. (2.10) given by the leaf width of the specific dipole being evolved.

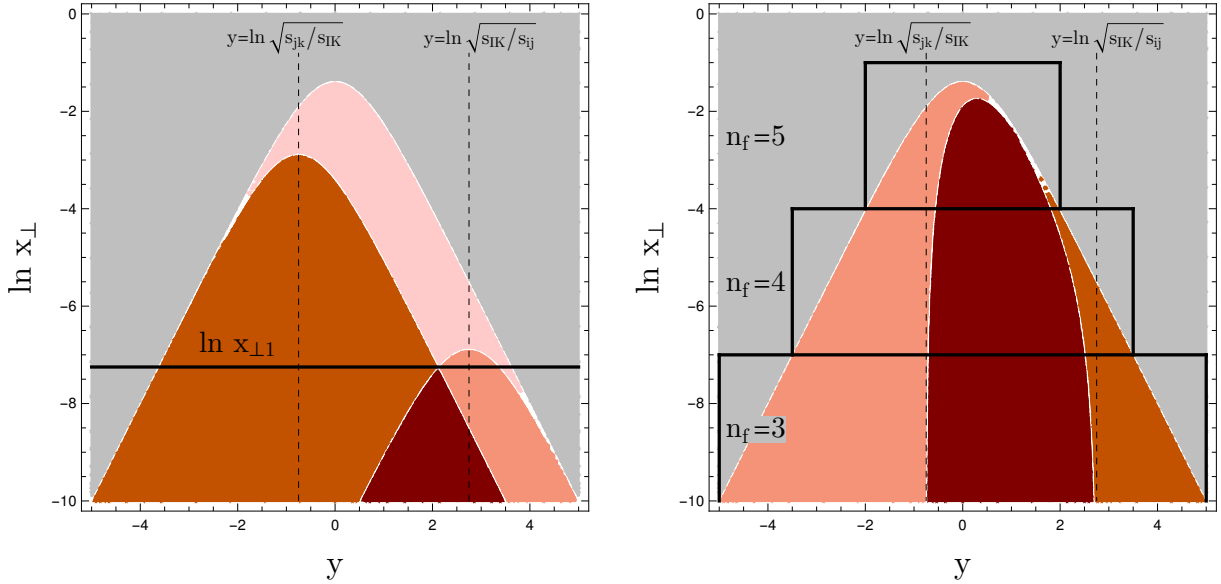


Figure 2: Lund-plane visualisation of the antenna-function phase-space, with constant contours in  $\ln x_{\perp}$ - $y$  variables. Left: Coloured pyramid structures depict the accessible phase-space planes at various stages in the evolution of massless partons. The largest ‘back-plane’ is the initial phase-space of the Born-level dipole with invariant  $s_{IK}$ . The black horizontal line is the value of  $x_{\perp}$  at which the first emission from this dipole occurs at. Below this scale there are now two dipoles, with invariant mass  $s_{jk}$  and  $s_{ij}$ , to the left and right of the dark overlap region respectively. The vertical dashed lines are the midpoint rapidity values of each dipole, with the back-plane centered on  $y = 0$ . Right: Similar to left but now with one of the quarks being massive. The dipole midpoints become asymptotic phase-space boundaries, again depicted by vertical dashed lines. Arbitrary evolution windows are also introduced, representing the variation in  $n_f$ , which will be discussed in section 2.2.

The exact interval of the  $n$ -th dipole,  $y_{\pm}^{(n)}$ , is made more manageable with an overestimate  $\bar{y}_{\pm}^{(n)}$ ,

$$y_{\pm}^{(n)} = \pm \frac{1}{2} \ln \left[ \frac{1 + \sqrt{1 - 4x_{\perp n}}}{1 - \sqrt{1 - 4x_{\perp n}}} \right], \quad \bar{y}_{\pm}^{(n)} = \mp \ln \sqrt{x_{\perp n}} \quad \Rightarrow \quad \int_{\bar{y}_{-}(x_{\perp})}^{\bar{y}_{+}(x_{\perp})} dy = \ln x_{\perp n}, \quad (2.11)$$

where  $x_{\perp n} = p_{\perp}^2/s_n$ , with respect to the invariant of the dipole,  $s_n$ . The overestimate approximates each leaf as a triangle, with the correct distribution recovered by veto. Consequently, Eq. (2.10) becomes,

$$\begin{aligned} \mathcal{A}_{IK \rightarrow ijk}(x_{\perp 1}, x_{\perp 2}) &= f_{\lambda} \alpha_s \frac{\mathcal{C}}{2\pi} \int_{x_{\perp 1}}^{x_{\perp 2}} \frac{dx_{\perp}}{x_{\perp}} \ln(x_{\perp}), \\ &= f_{\lambda} \alpha_s \frac{\mathcal{C}}{2\pi} \int_{\ln x_{\perp 1}}^{\ln x_{\perp 2}} \ln x_{\perp} d \ln x_{\perp}, \\ &= f_{\lambda} \alpha_s \frac{\mathcal{C}}{4\pi} (\ln^2 x_{\perp 2} - \ln^2 x_{\perp 1}). \end{aligned} \quad (2.12)$$

Substituting into Eq. (2.3) yields the evolution equation for constant  $\alpha_s$ ,

$$\begin{aligned} R &= \exp \left[ -f_{\lambda} \alpha_s \frac{m_{IK}^2}{s_{IK}} \frac{\mathcal{C}}{4\pi} (\ln^2 x_{\perp 2} - \ln^2 x_{\perp 1}) \right], \\ \Rightarrow x_{\perp 2} &= \exp \left[ -\sqrt{\ln^2 x_{\perp 1} - \frac{4\pi}{\alpha_s f_{\lambda} \mathcal{C}} \frac{s_{IK}}{m_{IK}^2} \ln R} \right]. \end{aligned} \quad (2.13)$$

## 2.2 Running Coupling and Evolution Windows

We now describe how to include the scale dependence of  $\alpha_s$ . Our simple Vincia algorithm will use one-loop running in the strong coupling. This is achieved by overestimating the rapidity range with the ‘Lund rectangle’, which is itself an overestimate of the Lund triangle. Fig. 2 demonstrates how a stack of Lund-rectangles are used to partition the phase-space into so-called ‘evolution windows’. The baseline of each window is defined by used-selected momentum values  $\bar{x}_\perp = \bar{p}_\perp^2/s_{\text{CM}}$ , with respect to shower CM-scale. The rapidity range (window width) within a window  $\Delta y(\bar{x}_\perp)$  is then given by

$$y_\pm(\bar{x}_\perp) = \pm \frac{1}{2} \ln \left( \frac{1 + \sqrt{1 - 4\bar{x}_\perp}}{1 - \sqrt{1 - 4\bar{x}_\perp}} \right),$$

$$\Delta y(\bar{x}_\perp) = y_+(\bar{x}_\perp) - y_-(\bar{x}_\perp). \quad (2.14)$$

The baselines of the evolution windows,  $\bar{x}_\perp$ , can be selected arbitrarily. However, an efficient balance should be found which minimises the frequency of transition between windows, while not excessively overestimating the rapidity ranges. The default choice in Vincia is to use the quark-mass thresholds as the baselines, so that  $n_f$  changes from window to window. This is convenient, as a running coupling requires that we vary  $n_f$  anyway.

The  $x_\perp$  dependence of the strong coupling is given by

$$\alpha_s(x_\perp) = \frac{1}{b_0 \ln(x_\perp/x_\Lambda)}, \quad \text{where} \quad x_\Lambda = \frac{\Lambda_{n_f}^2}{k_{RSIK}}. \quad (2.15)$$

$k_R$  is the renormalisation scale parameter which we set to unity in this work [36].  $\Lambda_{n_f}$  is the Landau pole, which depends on the number of quark flavours  $n_f$ . We will discuss its explicit form shortly.  $b_0$  is the one-loop running coefficient, written in terms of  $n_f$  and the colour-Casimirs  $C_A$ ,  $T_R$ ,

$$b_0(n_f) = \frac{11C_A - 4T_R n_f}{12\pi}. \quad (2.16)$$

The evolution windows allow for the removal of the explicit  $x_\perp$  dependence within the rapidity interval. This enables integration over the logarithmic structure of  $\alpha_s(x_\perp)$  instead,

$$\begin{aligned} \mathcal{A}_{IK \rightarrow ijk}(x_{\perp 1}, x_{\perp 2}) &= \frac{I_E}{b_0} \int_{x_{\perp 1}}^{x_{\perp 2}} \frac{dx_\perp}{x_\perp} \frac{1}{\ln(x_\perp/x_\Lambda)}, \\ &= \frac{I_E}{b_0} \int_{\ln x_{\perp 1}/x_\Lambda}^{\ln x_{\perp 2}/x_\Lambda} \frac{d \ln(x_\perp/x_\Lambda)}{\ln(x_\perp/x_\Lambda)}, \\ &= \frac{I_E}{b_0} \left( \ln \ln \left( \frac{x_{\perp 2}}{x_\Lambda} \right) - \ln \ln \left( \frac{x_{\perp 1}}{x_\Lambda} \right) \right). \end{aligned} \quad (2.17)$$

$I_E$  is the so-called ‘evolution coefficient’, which contains the following terms,

$$I_E = f_\lambda \frac{\mathcal{C}}{2\pi} \Delta y(\bar{x}_{\perp 1}). \quad (2.18)$$

Eq. (2.17) can be rearranged to obtain an expression for  $x_\perp$  which now accounts for the running of  $\alpha_s$ . We once again sample from the uniform distribution  $R \sim \mathcal{U}(0, 1)$ , by solving  $R = \exp(-\mathcal{A})$ . This yields the evolution equation with running- $\alpha_s$ ,

$$x_{\perp 2} = x_\Lambda \left( \frac{x_{\perp 1}}{x_\Lambda} \right)^{R^{(b_0/I_E)}}. \quad (2.19)$$

We emphasise that  $R$  is raised to the power of  $b_0/I_E$ .

The next step is to calculate  $\Lambda_{n_f}$ , needed in the calculation of  $x_\Lambda$ .  $n_f$  depends on the  $p_{\perp}^2$ -scale, since the phase space can shrink to the point where some quark masses are inaccessible. In our present context of  $Z^0$ -decay we have  $n_f = 5$ , since the starting scale  $m_Z^2$  is less than the top-quark scale  $m_t^2$ .  $\Lambda_5$  can be determined from experimental measurements of the strong coupling at the  $Z$ -mass scale;

$$\begin{aligned} \alpha_s(m_Z^2) \approx 0.1185 &= \frac{1}{b_0(5) \ln(m_Z^2/\Lambda_5^2)}, \\ \Rightarrow \Lambda_5 &\approx 0.088 \text{ GeV}. \end{aligned} \quad (2.20)$$

However, only  $\Lambda_5$  can be calculated this way, otherwise the transition from  $\Lambda_5 \rightarrow \Lambda_4$  and  $\Lambda_4 \rightarrow \Lambda_3$  will be discontinuous. Continuity is restored by calculating  $\Lambda_4$  with respect to  $\Lambda_5$ , and so-on.

$$\Lambda_4 = \Lambda_5 \left( \frac{m_b}{\Lambda_5} \right)^{2/25} \quad \Lambda_3 = \Lambda_4 \left( \frac{m_c}{\Lambda_4} \right)^{2/27}. \quad (2.21)$$

Vincia treats up, down and strange quarks as massless, and most parton showers will terminate at the hadronisation scale before they reach the two-flavour threshold and below. Hence we typically only need  $\Lambda_5$ ,  $\Lambda_4$  and  $\Lambda_3$ .

Finally, after generating the new  $x_{\perp 2}$  value, we need to check its validity. If invalid, we need to veto  $x_{\perp 2}$ , the procedure for which we defer to the following section. We may also need to update the evolution window if  $x_{\perp 2}$  is less than the current baseline  $\bar{x}_{\perp 1}$ . If this is the case we set  $x_{\perp 2} \rightarrow x'_{\perp 1} = \bar{x}_{\perp 1}$ , update  $n_f$  and  $I_E$  for the new window, and then generate a  $x'_{\perp 2}$  using  $x'_{\perp 1}$ . We may also terminate the shower if  $p_{\perp 2}^2$  is less than a user defined cut-off scale  $p_{\perp 1 \text{Had}}^2$ .

### 2.3 Generating New Partons

The previous sections describe the generation of a ‘branching scale’ for the emission of a new parton in a  $2 \rightarrow 3$  process. In this section, we describe how this parton is created, and how this changes the event. We begin by building some intuition for how the shower evolves.

Our simplified discussion is centered on the initial process  $Z^0 \rightarrow q\bar{q}$ , which creates the initial quark-antiquark dipole. The phase space for this dipole is visualised with the primary Lund-plane in Fig 2. We are only considering gluon emission, so there is only one possible initial branching,  $q\bar{q} \rightarrow qq\bar{q}$ , generalised as  $IK \rightarrow ijk$  where  $j$  is the new gluon. We use the evolution equation to generate a  $x_\perp$  scale for this emission, moving down the Lund-plane. This produces two dipoles,  $qg$  and  $g\bar{q}$ , both of which can produce a gluon. We therefore require a method to select which dipole pair should produce an emission, which we call the ‘brancher’. We also need to generalise this to an arbitrary number of dipoles as the multiplicity grows for each subsequent emission.

Fig. 2 depicts the secondary phase-space leaves for these two dipoles. Since Vincia is a transverse momentum ordered shower, we impose the requirement  $p_{\perp 2}^2 < p_{\perp 1}^2$ . This makes the regions of the secondary leaves above  $\ln x_{\perp 1}$  inaccessible when generating  $x_{\perp 2}$ , which is accounted for in the evolution equation.

At a given shower-wide scale  $p_{\perp 1}^2$  each of the  $n$  dipoles will have some probability to become the brancher, which depends on the invariant  $s_n$  unique to each dipole. We emphasise that we select the brancher at the initial scale  $x_{\perp 1}$  and *then* generate a scale  $x_{\perp 2}$  at which the emission occurs. The brancher probability is given by the evolution coefficient which we introduced

in Eq. (2.18). Here we write the coefficient for the  $n$ -th dipole explicitly in terms of  $\bar{p}_{11}^2$ , the evolution-window baseline for  $p_{11}^2$ ,

$$I_E^n(\bar{p}_{11}^2, s_n) = f_\lambda^n \frac{C_n}{2\pi} \Delta y(\bar{x}_{11}^n), \quad \text{where} \quad \bar{x}_{11}^n = \frac{\bar{p}_{11}^2}{s_n}. \quad (2.22)$$

The Källén factor depends on the specific dipole invariants and the colour factor is given by one of the three relevant processes;

$$q\bar{q} \rightarrow qq\bar{q}: \mathcal{C} = 2C_F, \quad gg \rightarrow ggg: \mathcal{C} = C_A, \quad qq \rightarrow qgg: \mathcal{C} = \frac{2C_F + C_A}{2}. \quad (2.23)$$

The latter is an average of the  $q\bar{q}$  and  $gg$  dipole colour-factors, which also applies to the  $g\bar{q} \rightarrow gg\bar{q}$  case. This assumes the leading-colour limit, meaning more sophisticated treatments can also be implemented [37].

Once all the dipoles at the scale  $p_{11}^2$  have been assigned an evolution coefficient, the brancher is selected at random depending on the relative weights of each  $I_E^n$ . This can be implemented with a weighted linear-search algorithm or similar. The invariant of the brancher becomes the parent invariant,  $s_{IK} = s_n$ .

The next step is to determine the invariants of the post-branching partons  $ijk$ , to which we assign the two new dipoles created after the branching. They are calculated with the inverse mapping;

$$s_{ij} = s_{IK} e^{-\bar{y}_2} \sqrt{x_{12}} \quad s_{jk} = s_{IK} e^{\bar{y}_2} \sqrt{x_{12}}, \quad s_{ik} = s_{IK} - s_{ij} - s_{jk}. \quad (2.24)$$

Here,  $\bar{y}_2$  is a trial rapidity generated uniform at random on the baseline interval  $\Delta y(\bar{x}_{11})$ ;

$$\bar{y}_2 \sim \mathcal{U}(y_-(\bar{x}_{11}), y_+(\bar{x}_{11})). \quad (2.25)$$

This trial rapidity needs to satisfy  $|\bar{y}_2| < y_+(\bar{x}_{11})$ . If it fails this check, a new brancher must be selected with at scale  $x_{12} \rightarrow x'_{11}$  and the process is repeated. Similarly, if the rapidity is accepted, it subsequently needs to pass the relevant Monte-Carlo accept-reject step;

$$P_{\text{accept}} = \frac{\bar{a}_{IK \rightarrow ijk}^0}{\bar{a}_{\text{trial}}^0} > R \sim \mathcal{U}(0, 1). \quad (2.26)$$

If  $P_{\text{accept}}$  is less than the uniform random number  $R$ , then we need to regenerate a new brancher at the scale  $x_{12} \rightarrow x'_{11}$ . The general form of the antenna function  $\bar{a}_{IK \rightarrow ijk}^0$  is given by

$$\bar{a}^0(s_{ij}, s_{jk}, s_{ik}) = \frac{2s_{ik}}{s_{ij}s_{jk}} - \frac{2m_I^2}{s_{ij}^2} - \frac{2m_K^2}{s_{jk}^2} + \frac{1}{s_{IK} + 4m_I m_K} \left( \frac{s_{ij}}{s_{jk}} + \frac{s_{jk}}{s_{ij}} \right). \quad (2.27)$$

There are many variants of this antenna function used for different branchers [26, 28, 38].

If the phase-space point  $(x_{12}, \bar{y}_2)$  passes the above tests, it is accepted and the brancher it belongs to is allowed to emit a gluon. In order to conserve momentum, we need to map the momenta of partons  $IK$  onto the post-branching momenta of  $ijk$ . We will discuss such kinematics maps in the following section.

The final step is to update the colour indices of the partons in order to maintain a notion of colour connection. Vincia uses the same convention as Pythia [39] in the large-colour approximation. To do this, we consider the initial  $Z^0 \rightarrow q\bar{q}$  process. The quark is assigned a colour-anticolour pair  $(101, 0)$ , as is the antiquark  $(0, 101)$ . The zero label indicates no

colour/anticolour, while 101 labels an arbitrary colour that is shared between the two quarks. The colours  $C$  matrices for the  $2 \rightarrow 3$  branching are updated as follows.

$$C_{Z^0 q\bar{q}} = \begin{bmatrix} Z^0 : & 0 & 0 \\ q : & 101 & 0 \\ \bar{q} : & 0 & 101 \end{bmatrix} \quad \rightarrow \quad C_{Z^0 qg\bar{q}} = \begin{bmatrix} Z^0 : & 0 & 0 \\ q : & 101 & 0 \\ g : & 102 & 101 \\ \bar{q} : & 0 & 102 \end{bmatrix} \quad (2.28)$$

Here, the gluon has colour 102-101, connecting it to the parent quarks. This naturally generalises for further emissions, with the addition of a colour index for each new gluon.

## 2.4 The Recoil Scheme

The final piece of the algorithm is the kinematics map, sometimes called the recoil scheme. This is the procedure by which we map the two-parton pre-branching momenta  $\{p_I, p_K\}$  to the three-parton post-branching momenta  $\{p_i, p_j, p_k\}$ . This updates the event by replacing the two dipole parents with three daughter-partons, two of which are the recoiled parents and one of which is the newly emitted third parton.

The simplest scenario we study is the initial  $Z^0$ -decay into a massless quark-antiquark dipole which proceeds to emit a gluon,  $Z^0 \rightarrow q\bar{q} \rightarrow qg\bar{q}$ . In this ‘trivial’ case the parent momenta  $p_I, p_K$  of the  $q\bar{q}$  pair are given by

$$p_I^q = \left( \frac{m_Z}{2}, 0, 0, \frac{m_Z}{2} \right) \quad (2.29)$$

$$p_K^{\bar{q}} = \left( \frac{m_Z}{2}, 0, 0, -\frac{m_Z}{2} \right), \quad (2.30)$$

where  $E_{cm} = m_Z$  is the center-of-mass energy of the initial hard process. These momenta are given in the rest frame of the  $Z^0$ -decay, which are typically defined as the ‘lab frame’. The momenta are necessarily anti-parallel, directed along the z-axis by convention.

The Vincia algorithm constructs  $\{p_i, p_j, p_k\}$  in the dipole-center-of-mass frame, then performs the necessary boosts and rotations to return back to the lab frame. This is done by constructing the momentum in an initial  $1 + 2$  dimensional frame, with no component in the  $\hat{y}$ -direction, which we instead reconstruct later. This so-called center-of-mass-z (CMz) frame orients parton  $i$  along the  $\hat{z}$ -axis. We then define the  $j$  and  $k$  partons with respect to  $i$  as follows.

$$\begin{aligned} p_i^\mu &= (E_i, 0, 0, p_i), \\ p_j^\mu &= (E_j, |\mathbf{p}_j| \sin \theta_{ij}, 0, |\mathbf{p}_j| \cos \theta_{ij}), \\ p_k^\mu &= (E_k, |\mathbf{p}_k| \sin \theta_{ik}, 0, |\mathbf{p}_k| \cos \theta_{ik}). \end{aligned} \quad (2.31)$$

This construction places the partons in an  $\hat{x}\hat{z}$ -plane, known as the ‘branching plane’. Using on-shell conditions, the energies and momenta of the three partons can be determined,

$$E_i = \frac{m_{IK}^2 - m_{jk}^2 + m_i^2}{2m_{IK}} \stackrel{m \rightarrow 0}{=} \frac{s_{IK} - s_{jk}}{2\sqrt{s_{IK}}} \quad |\mathbf{p}_i| = \sqrt{E_i^2 - m_i^2} \stackrel{m \rightarrow 0}{=} E_i, \quad (2.32)$$

$$E_j = \frac{m_{IK}^2 - m_{ik}^2 + m_j^2}{2m_{IK}} \stackrel{m \rightarrow 0}{=} \frac{s_{IK} - s_{ik}}{2\sqrt{s_{IK}}} \quad |\mathbf{p}_j| = \sqrt{E_j^2 - m_j^2} \stackrel{m \rightarrow 0}{=} E_j, \quad (2.33)$$

$$E_k = \frac{m_{IK}^2 - m_{ij}^2 + m_k^2}{2m_{IK}} \stackrel{m \rightarrow 0}{=} \frac{s_{IK} - s_{ij}}{2\sqrt{s_{IK}}} \quad |\mathbf{p}_k| = \sqrt{E_k^2 - m_k^2} \stackrel{m \rightarrow 0}{=} E_k, \quad (2.34)$$

with the fully massless case also given. Similarly the angles of partons  $j$  and  $k$  relative to  $i$  are given by

$$\theta_{ij} = \arccos \frac{2E_i E_j + m_i^2 + m_j^2 - m_{jk}^2}{2|\mathbf{p}_i||\mathbf{p}_j|} \stackrel{m \rightarrow 0}{=} \arccos \frac{2E_i E_j - s_{ij}}{2E_i E_j} \quad (2.35)$$

$$\theta_{ik} = \arccos \frac{2E_i E_k + m_i^2 + m_k^2 - m_{ik}^2}{2|\mathbf{p}_i||\mathbf{p}_k|} \stackrel{m \rightarrow 0}{=} \arccos \frac{2E_i E_j - s_{ik}}{2E_i E_j}. \quad (2.36)$$

The next step is to obtain the  $\hat{y}$ -values by performing two global rotations through Euler-angles  $\psi$  and  $\phi$ . The latter is a rotation out of the branching plane, around the  $\hat{z}$ -axis. Since we assume unpolarised partons and thus no spin correlations, this angle can be selected uniform at random;

$$\phi \sim \mathcal{U}(0, 2\pi). \quad (2.37)$$

The other angle  $\psi$  contains the remaining physics of the actual recoil process. It is global rotation in the branching plane (around the  $\hat{y}$ -axis) which determines how much the momenta  $\{p_i, p_j, p_k\}$  are changed with respect to  $\{p_I, p_K\}$ . This rotation is modelled by the  $r$ -parameter;

$$r = \frac{s_{jk}}{s_{ij} + s_{jk}}. \quad (2.38)$$

This is the canonical definition introduced in [9, 30], which enables smooth mapping between the collinear limits. The collinear limits of traditional DGLAP based showers are recovered for  $r = 0$  ( $s_{jk} \rightarrow 0$ ) and  $r = 1$  ( $s_{jk} \rightarrow 0$ ).

In the massless case, the  $\psi$  angle is defined in terms of invariants and the  $r$ -parameter [21],

$$\begin{aligned} \rho &= \sqrt{1 + \frac{4r(1-r)y_{ij}y_{jk}}{y_{ik}}}, \\ y_{Ii} &= -\frac{(1-\rho)y_{ik} + 2ry_{ij}y_{jk}}{2(1-y_{ar})}, \\ \psi &= 1 + \frac{2y_{Ii}}{1-y_{rb}}. \end{aligned} \quad (2.39)$$

The massless description is provided within [26]. The full center-of-mass momenta  $p_{\text{CM}}^\mu$  (with  $y$ -component) can thus be obtained by applying a general 3D rotation  $R_{\phi\psi}$  to the CMz-frame momenta from Eq. (2.31);

$$p_{\text{CM}}^\mu = R_{\phi\psi} p_{\text{CMz}}^\mu. \quad (2.40)$$

The final step is to transform the CM-frame momenta to the lab frame with an appropriate Lorentz boost  $\Lambda_\nu^\mu$ . Such a transformation matrix is defined by the frame spanned by  $p_I^\mu$  and  $p_K^\mu$  (in the lab frame). Thus the complete kinematics map can be defined by the sequence of transformations

$$p_{\text{lab}}^\mu = \Lambda_\nu^\mu R_{\phi\psi} p_{\text{CMz}}^\nu. \quad (2.41)$$

With the post-branching four-momenta now defined, the event record can be updated by replacing  $\{p_I^\mu, p_K^\mu\}$  with  $\{p_i^\mu, p_j^\mu, p_k^\mu\}$ . This is typically done with direct replacements,  $p_I^\mu \rightarrow p_i^\mu$  and  $p_K^\mu \rightarrow p_k^\mu$  followed by the insertion of  $p_j^\mu$  in-between.

### 3 The Accuracy of the Vincia Antenna-Shower

Following our introduction and implementation of the Vincia antenna-shower, we now seek to analyse its accuracy. To achieve this we first need a definition of the accuracy of a parton shower. One can always make comparisons to experimental data, but this is a holistic approach which tends to obscure specific systematic shortcomings we are interested in resolving. In the context of collider observables, one typically attempts to assess the order in perturbation theory which the quantity is accurate to. While the parton shower generates an observable at arbitrary order in  $\alpha_s$ , the antenna functions only capture the leading contribution at a given order. One therefore needs a description for this order-by-order accuracy. A stated goal of the PanScales event generator [40] is to establish such a definition for parton showers.

#### 3.1 Logarithmic Accuracy

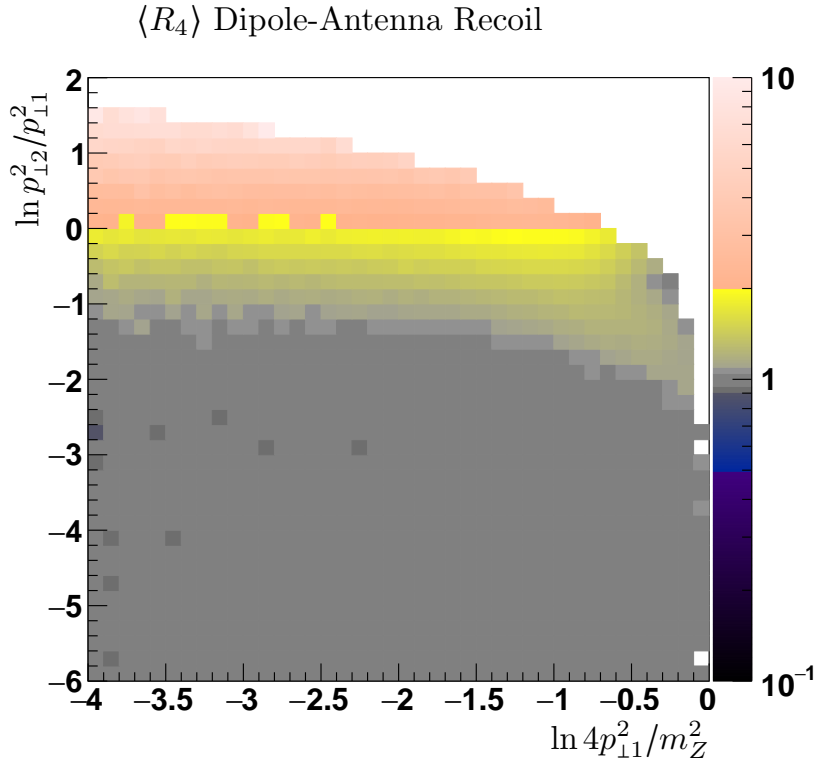


Figure 3: Geometric-mean for the ratio  $\langle R_4 \rangle$  between the analytically calculated four-parton squared matrix-element of a  $3 \rightarrow 4$  process and the parton-shower approximation to that process.  $\langle R_4 \rangle$  is represented as a 2D histogram of phase-space parameterised by the hardness of the first and second gluons emitted with the default Vincia dipole-antenna kinematics, using the Ariadne  $p_{\perp} = s_{ij}s_{jk}/s_{IK}$  definition. Ratios near unity indicate good agreement, while variation from unity indicate inaccuracy. Phase space points were generated with the RAMBO [50, 51] sampler, and matrix elements were calculated with MadGraph5 [41].

To construct such a definition, recall that the universal singularity structure of QCD processes is present at all orders of the parton-shower evolution, made manifest by the divergent antenna functions. Integrating these singularities between two scales  $Q_1^2$  and  $Q_2^2$  results in logarithms of ratios of those scales;

$$\int_{Q_1^2}^{Q_2^2} \left[ \alpha_s \left( \frac{1}{s_{ij}s_{jk}} + \text{subleading} \right) \right]^n ds_{ij} ds_{jk} = \alpha_s^n \left[ \underbrace{\ln \left( \frac{Q_2^2}{Q_1^2} \right)^{2n}}_{\text{double-log}} + \text{subleading logarithms} \right]. \quad (3.1)$$

Here we integrate the  $n$  soft-eikonal terms associated with an arbitrary  $n$ -parton topology. Additional subleading terms are also included, which contribute subleading logarithms of lesser power than the leading  $\ln^{2n}$  double logarithm.

The ‘logarithmic accuracy’ of the shower thus refers to the number of these logarithms which are correctly generated by the evolution. If all the terms are accounted for, the series will converge on the true result for the given observable, agreeing with the matrix-element calculation at the given  $\mathcal{O}(\alpha_s^n)$ . Leading-logarithmic showers are typically capable of reproducing the double-logarithmic term, along with the  $\ln^{2n-1}$  term [42]. Most contemporary parton-showers, including Vincia, may thus be considered leading-log (LL) since they are capable of generating the logarithms associated with the soft-eikonal term. Whether these showers are capable of next-to-leading logarithmic (NLL) accuracy is less clear.

The logarithmic accuracy of a shower is established by making comparisons to established analytic results. The technique of ‘analytic resummation’ allows for the exact calculation of a shower observable to a given logarithmic accuracy. The advantage of this method is its unambiguous definition of accuracy, since the observable is resummed as a series of logarithms, much like Eq. (3.1). The disadvantage is that a different resummation is required for each shower observable [43]. The parton shower is evolved at the integral level, before logarithms are generated, and is thus capable of describing a wide variety of different observables. This comes at the cost of ambiguity about the accuracy of any given shower observable.

The logarithmic accuracy of Vincia may thus be assessed by isolating logarithmic contributions and comparing them to the equivalent results from analytic resummation, The studies of which are ongoing for Vincia. The contribution of this work to these studies will be discussed in the following section.

Such studies have been performed with the PanScales and Alaric event generators [11, 44]. The results suggest that so-called ‘local’ recoil schemes are associated with subleading-logarithmic inaccuracy. The Vincia kinematic map introduced in section 2.4 is an example of a local recoil scheme, as recoil is distributed amongst just two of the partons in the event. Likewise ‘global’ recoil schemes assign recoil to all partons in the event, and are therefore less sensitive to these effects.

To understand these results, recall that the kinematics map is responsible for evolving the accessible phase space as the shower progresses. Heuristically, this alters the domain of integration, affecting the logarithmic structure even if the antenna functions contain the necessary NLL singularities. Consequently, the chosen recoil scheme can affect the agreement with resummed results.

In the soft-collinear regions of phase space, the dipole-antenna kinematics map will correctly distribute recoil amongst the dipole parents. Outside these regions however, no such guarantee exists. As an example, consider a hard, wide-angle emission. The hardness of this emission ensures that the recoil given to the parents will be significant, and the wide angle implies this recoil will be largely transverse to the parents current momenta. Since there are only two partons absorbing this recoil, the emission will non-trivially alter the topology of the event, essentially ‘kicking’ the partons too hard. Global recoil schemes tend not to suffer

from this problem, since the recoil is distributed amongst all partons in the event, and hence each individual recoil is small.

We can heuristically derive the logarithmic inaccuracy associated with hard, wide-angle emission. Consider integrating an antenna function which contains the leading eikonal term as well as two subleading singular terms,

$$\int_{x_{11}}^{x_{12}} dy_{ij} dy_{jk} \left[ \frac{1}{y_{ij} y_{jk}} - \underbrace{\frac{y_{jk}}{y_{ij}} - \frac{y_{ij}}{y_{jk}}}_{\text{subleading}} \right] = \int_{x_{11}}^{x_{12}} \int_{y^-}^{y^+} dx_{\perp} dy \left[ \frac{1}{x_{\perp}} - 2 \cosh(2y) \right] = \Delta y \ln \frac{x_{12}}{x_{11}} + 2(x_{11} - x_{12}) \sinh \Delta y, \quad (3.2)$$

where we transform variables and define an arbitrary rapidity range  $\Delta y$ . Strongly-ordered emissions,  $x_{12} \ll x_{11}$ , are favoured by the soft singularity, which ensures that the logarithm associated with the eikonal term will dominate the above result. For hard, wide-angle emissions the momentum scales may still be ordered, but become commensurate;  $x_{11} \sim x_{12}$ . In this scenario, both terms in the expression will now be small. Therefore hard, wide-angle emissions are suppressed relative to soft-collinear radiation. Nevertheless, the logarithmic term no longer dominates the expression, which is now sensitive to subleading effects. Since the kinematics map is only designed to describe the phase space of the first term, the correct rapidity range  $\delta y$  and dipole invariants are not guaranteed for the second, subleading term.

The inaccuracy associated with hard, wide-angle emission may be demonstrated numerically by plotting the ratio between the parton shower and the analytical matrix element for such emissions. The geometric mean for this ratio may be plotted across a survey of phase space, where deviation from unity indicates a shortcoming of the parton shower approximation. This is depicted in Fig. 3, where each bin is defined by the ratio

$$\langle R_4 \rangle = \left\langle \frac{|\mathcal{M}_3|^2}{|\mathcal{M}_4|^2} a_{\text{sector}}^0(y_{ij}, y_{jk}) \right\rangle. \quad (3.3)$$

The observed shape of the distribution is the consequence of the kinematic constraint  $4p_{11}^2 < m_{\text{CM}}^2$ . Importantly, if  $p_{12}^2 \ll p_{11}^2$ , the emission is sufficiently soft to suppress any subleading disagreement, since  $\langle R_4 \rangle \sim 1$ . As the emissions become harder, the expected departure from unity is observed. The parton-shower approximation begins overestimating the matrix element in the commensurate momenta region  $p_{12}^2 \sim p_{11}^2$ .

### 3.2 Attempting a Numerical Study

We now attempt to establish a systematic framework for assessing logarithmic accuracy of the Vincia dipole-antenna shower. However, this proves challenging, and is the necessary subject of further investigation. Nevertheless, we outline the work that was undertaken, in the hope that future studies may build upon these foundations.

In order to make comparisons with analytically resummed observables, the logarithmic contributions to a parton-shower observable must be isolated, term-by-term. This is achieved by suppressing all but the LL and NLL terms, using the limit  $\alpha_s \rightarrow 0$ . In this limit the evolution equation will produce ultra-soft radiation, resulting in large hierarchies between the scales  $Q_2^2$  and  $Q_1^2$ , causing the logarithms to diverge. Once the logarithms reach  $\mathcal{O}(1/\sqrt{\alpha_s})$ , Eq. (3.1) will take the form

$$\underbrace{1 + \sqrt{\alpha_s}}_{\text{LL}} + \underbrace{\alpha_s + \alpha_s \sqrt{\alpha_s} + \dots}_{\text{NLL}}. \quad (3.4)$$

For sufficiently small  $\alpha_s$ , the beyond-NLL contributions can be neglected, resulting in pure NLL observables, which are then compared to analytically resummed results.

However, these small- $\alpha_s$  studies pose several problems for existing parton shower algorithms. A shower with a truly vanishing coupling constant will not evolve at all, since there is no interaction between the fields. Instead, several small but non-vanishing values of  $\alpha_s$  may be studied such that the true  $\alpha_s \rightarrow 0$  limit may be extrapolated.

This ultra-soft radiation poses an immediate complication regarding numerical stability. Vincia uses double floating-point precision, implying sums between values which differ by more than sixteen orders of magnitude are liable to instability. Take for example Eq. (2.39), the  $\rho$  parameter in the kinematics map:

$$\rho = \sqrt{1 + \frac{4r(1-r)y_{ij}y_{jk}}{y_{ik}}}. \quad (3.5)$$

The ratio inside the radical approaches zero in the small- $\alpha_s$  limit, since  $y_{ik} \gg \{y_{ij}, y_{jk}\}$ . At double-precision the computer will consequently consider this equation to be unity, which sabotages the kinematics map.

Similar issues exist at all stages within the kinematics map. In some cases it was possible to stabilise equations with a careful reconstruction which avoided these instabilities. However, the requisite rotation and boost to the lab frame in Eq. (2.41) typically remained unstable. A possible solution is a Lorentz-invariant kinematics map. Such a recoil scheme would not require unstable transformations between frames.

A Lorentz-invariant reformulation of the original dipole-antenna map [30] was investigated, however the problem is notoriously challenging. For the purposes of the Vincia antenna shower, the pre and post-branching momenta are related by

$$\begin{aligned} p_I &= xp_i + rp_j + zp_k, \\ p_K &= (1-x)p_i + (1-r)p_j + (1-z)p_k, \end{aligned} \quad (3.6)$$

where  $r$  is the canonical parameter introduced in Eq. (2.38), and expressions for  $x$ ,  $z$  are presented in [26]. A frame-independent  $3 \rightarrow 2$  ‘clustering map’ is straightforward to derive, as there are less degrees of freedom in the pre-branching topology than the post-branching. Inverting this map for the purposes of  $2 \rightarrow 3$  branching is less straightforward, since the system is underdetermined. It was brought to the authors attention that the work of Kosower & Page [45] had concurrently achieved an inverse kinematics map. However, this map was not immediately suitable for the Vincia algorithm, and given its considerable complexity, its implementation was deemed beyond the time frame of this work.

Furthermore, following personal communication with C. Preuss<sup>1</sup> and S. Höche<sup>2</sup> it became clear that some separate success had been made in stabilising the Vincia recoil map for the purpose of these small- $\alpha_s$  studies. This map was implemented in a prototype, quadruple-precision version of Vincia with many modifications to stabilise the algorithm. The results from these tests are yet to be published, but they indicate that the current form of the Vincia dipole-antenna kinematics map will not be NLL accurate in all regions of phase space.

In light of these technical challenges, a complete numerical study of the logarithmic accuracy of Vincia was deemed unfeasible for the existing scope of this project. All the necessary components needed to stabilise the algorithm have been presented in section 2, and it is the authors intention that they are made clear for future studies. Nevertheless, we instead proceed to directly study the performance of the dipole-antenna kinematics map for hard, wide-angle emissions.

<sup>1</sup>(28th Nov 2022, 16th March 2023) [Orcid](#).

<sup>2</sup>(28th Nov 2022) [Orcid](#).

## 4 Novel Jet-Antenna Kinematics

While a full assessment of the logarithmic accuracy of Vincia requires further development, we still find some guiding principles in the previous section. The shortcomings associated with dipole-antenna kinematics were made apparent within Fig. 3. In this section we propose a simple extension of this recoil scheme, intended to improve upon these deficiencies. We wish to reflect the advantages of global recoil schemes, while retaining the  $2 \rightarrow 3$  formalism which underpins the Vincia algorithm. The novel ‘jet-antenna’ kinematics map is introduced herein as a proof of concept. We also explore avenues for extension and future developments which were outside the scope of this work.

### 4.1 Motivating Jet Recoil

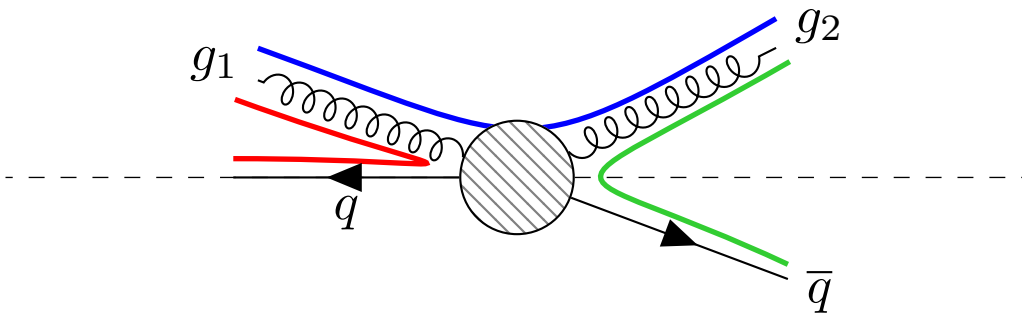


Figure 4: Four-parton topology depicting the emission of two gluons from a quark dipole, including colour lines in the leading-colour approximation. Gluon  $g_2$  is explicitly the second emission gluon, radiated from the  $g_1\bar{q}$  dipole.  $g_2$  is not emitted collinear to  $g_1$  or  $\bar{q}$ .

Consider a simple four-parton topology as depicted in Fig. 4. We will impose ordering such that  $p_1^2(g_1) > p_1^2(g_2)$ , using the Ariadne momentum definition.  $g_2$  may be considered a wide-angle emission for our purposes.

By default, Vincia would generate the emission of  $g_2$  with local recoil, distributing transverse momentum to  $g_1$  and  $\bar{q}$  only, leaving  $q$  unchanged. Global recoil schemes would instead incorporate the quark, and consequently the transverse recoil on  $g_1$  and  $\bar{q}$  will be diminished accordingly. In the case of soft emission, this recoil will be negligible for both local and global kinematics. In the case of hard emission however, the recoil will be significant and the final topology would depend strongly the chosen recoil scheme.

Furthermore, dipole-antenna kinematics rely implicitly on the leading-colour approximation. In such a limit, the colour flow within the event is represented as a planar diagram, as in Fig. 4, where colour lines do not intersect [46]. In a full-colour description of QCD however, one would account for the coherent contribution from all radiators in the event [47, 48]. Such a model would require a multipole description of QCD, a capability which remains elusive for parton showers [49]. Nevertheless, since global recoil schemes incorporate all radiators during the emission of a parton, they reflect the full-colour description to a greater extent than local schemes do.

The advantage of the dipole-local description lies in the simple phase-space factorisation which facilitates the simple factorisation of universal matrix-element ratios into the antenna functions. Global recoil schemes are not a-priori compatible with such factorisation, making it inadequate to simply swap the kinematics map for a global one. To achieve a ‘global-esque’ dipole-antenna kinematics map, there are several desirable features;

- The map should retain the  $IK \rightarrow ijk$  structure of the existing kinematics map, as described in section 2.4.
- However, the dipole parents  $I$  and  $K$  may consist of more than one parton. Such a collection of partons may be referred to as a ‘jet’.
- These jets will thus participate in regular dipole-antenna recoil, and enter the final state as the post-branching pseudo-particles  $i$  and  $k$ .
- A suitable method must be selected for how to collect partons into a jet, and how to separate them once more after recoil.

Consider as an example, the combination of partons  $q$  and  $g_1$  into a jet ( $qg_1$ ). This would remove the red colour-connection depicted in Fig. 4. The second emission gluon  $g_2$  can then be radiated from the  $(qg_1)\text{-}\bar{q}$  dipole, allowing for  $q$  to participate in the recoil when it otherwise would have spectated.

Such a removal of the colour line must be treated with care. A full-colour description of the emission of  $g_2$  would incorporate all colour charges in the event, however we have now explicitly removed one. We must thus consider the scenarios where this is acceptable. If all the partons in the event are ‘well separated’ (not collinear) with respect to each other, then the charge-anticharge endpoints of the colour line will be clearly distinguishable in the resulting field coherence which produces  $g_2$ . Furthermore, the combination of two or more of these well separated partons into a jet will drastically alter the charge distribution. Conversely, if the partons which form the jet are largely collinear, the colour-dipole endpoints will interfere destructively, and won’t contribute to the emission of  $g_2$ . Provided the emitted gluon is well separated from such a jet, the overall charge configuration will remain approximately the same.

We hence do not expect these jet recoils to outperform regular dipole-local kinematics in all configurations. Studies must be performed to determine the cases where they are advantageous. We begin with a description of the kinematics map itself, followed by some preliminary numerical results which survey a number of phase-space variables.

## 4.2 The Jet-Antenna Kinematics Map

For now, let us restrict ourselves to the four-parton topology depicted in Fig. 4. We want a recoil scheme which incorporates the spectator parton  $q$ . The simplest method to achieve this is to sum the four momenta of the jet constituents:

$$p_{\text{jet}}^\mu = p_q^\mu + p_{g_1}^\mu, \quad m_{\text{jet}}^2 = 2p_q^\mu p_{g_1\mu} = s_{qg_1}. \quad (4.1)$$

This necessarily introduces a mass to the jet, which implies a massive kinematics map should be employed, even if all the constituent partons are massless. Due to its simplicity, this will be the method used to construct jets in this work.

In the context of a shower algorithm, this jet can now be used to generate a new parton with the regular dipole-antenna  $2 \rightarrow 3$  kinematics map. The evolution equation would be used to generate a phase space point for this emission, based on the  $(qg_1)\text{-}\bar{q}$  dipole. Dipole-local recoil could then be applied to the jet as a whole, allowing for  $q$  to recoil when it otherwise would have been neglected. We label the pre-branching jet momenta  $\tilde{p}_{\text{jet}}^\mu$ , and the post-branching jet  $p_{\text{jet}}^\mu$ .

We then construct the Lorentz-transformation matrix which takes  $\tilde{p}_{\text{jet}}^\mu$  to  $p_{\text{jet}}^\mu$ . This transformation may then be applied to the jet constituent particles in the pre-branching state,  $\tilde{p}_q^\mu$

and  $\tilde{p}_{g_1}^\mu$ . Such a transformation maps those momenta onto the post-branching state, while conserving momentum. We have thus incorporated the spectator parton into the recoil, while still retaining the  $2 \rightarrow 3$  kinematics map.

The same technique may be used for the inverse of the kinematics map, where a  $3 \rightarrow 2$  ‘clustering’ process. The jet is created and mapped with a the corresponding inverse Lorentz-transformation.

### 4.3 Numerical Analysis

In this section we compared the performance of the novel jet-antenna recoil scheme with the default dipole-antenna kinematics map. This analysis proceeded using the matrix-element ratio  $\langle R_4 \rangle$  introduced in Eq. (3.3). The RAMBO [50, 51] uniform phase-space sampler generated four-parton topologies from a  $m_Z = 91.188$  GeV process. These raw events contained two quarks and two gluons. The following two ratios were calculated for comparison.

$$\langle R_4^{\text{dip}} \rangle = \left\langle \frac{|\mathcal{M}_3^{\text{dip}}|^2}{|\mathcal{M}_4|^2} a_{\text{sector}}^{\text{dip}}(y_{ij}, y_{jk}) \right\rangle, \quad \langle R_4^{\text{jet}} \rangle = \left\langle \frac{|\mathcal{M}_3^{\text{jet}}|^2}{|\mathcal{M}_4|^2} a_{\text{sector}}^{\text{jet}}(y_{ij}, y_{jk}) \right\rangle \quad (4.2)$$

The labels ‘dip’, and ‘jet’ indicate the clustering was performed with dipole-antenna and jet-antenna recoil schemes respectively. The MadGraph5 package [41] was used to calculate the matrix elements. The four-parton matrix element was the baseline for comparison between the two cases. The relevant antenna function was included to complete the parton-shower approximation to  $|\mathcal{M}_4|^2$ . Specifically, sector antenna-functions were used to reduce the number of permutations under consideration [38].

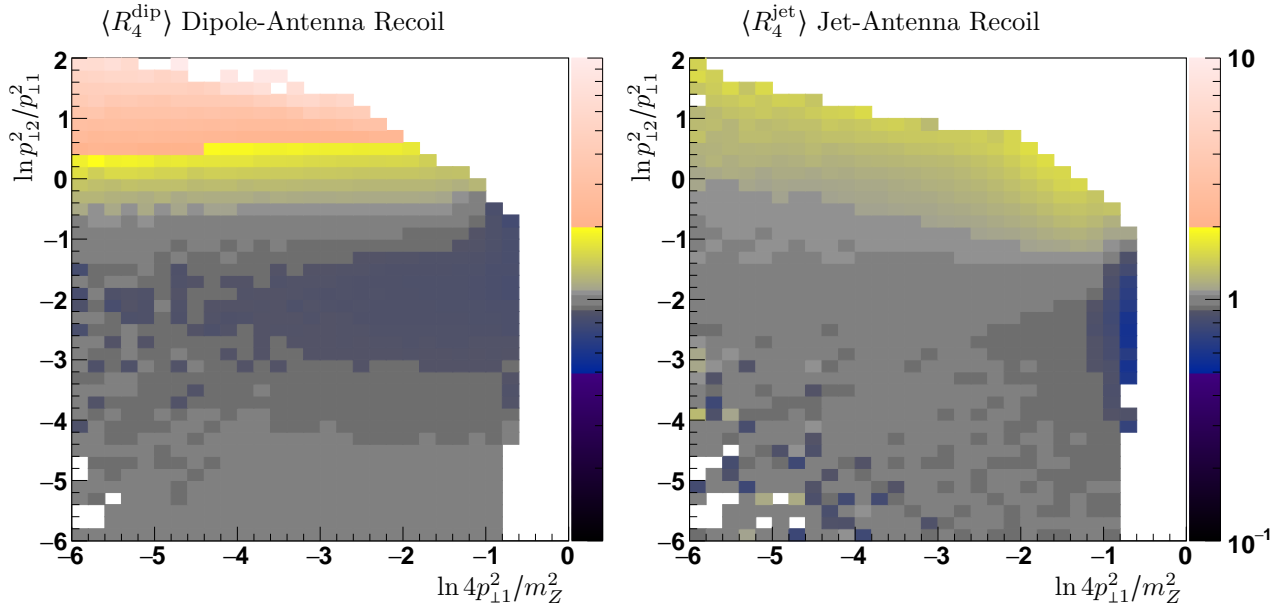


Figure 5: Left:  $\langle R_4^{\text{dip}} \rangle$  across phase space parameterised by the hardness of  $g_1$  and the hardness of  $g_2$  with respect to  $g_1$ . Colour lines are not crossed in these samples, and both gluons must be separated by at least one unit of rapidity. Right:  $\langle R_4^{\text{jet}} \rangle$  for the same configuration as left. White pixels were not filled, either due to kinematic constraints or rarity.

For the dipole-antenna case, the gluon with the smallest Ariadne  $p_1^2$  was clustered, which is a requirement of the sector antenna functions. Quark-gluon antenna functions were used for the  $qgg \rightarrow qg$  and  $gg\bar{q} \rightarrow g\bar{q}$  clusterings. For the jet-antenna case, the jet is treated as a quark, since the internal colour line with the gluon is removed. Hence, quark-quark antenna functions were used, which importantly do not contain gluon singular terms.

Finally, some restrictions were placed on the rapidities of the partons in the event. Using the intuition developed in section 4.1, it was expected that jet kinematics would be highly sensitive to the angular configuration of the partons in the event, and unsuitable for some regions of phase space. Furthermore, the uniform sampling of phase space permitted many pathological topologies which would be suppressed by an actual event generator. The following two conditions were imposed such that the results were interpretable, while remaining suitable as simple criteria for jet kinematics.

1. The rapidity differences  $\Delta y_{12}$ ,  $\Delta y_{23}$ ,  $\Delta y_{34}$  between the four partons in the event,  $1234 = qgg\bar{q}$ , must all have the same sign. This ensures that colourlines are not ‘crossed’, such that all clustered partons remained outside the opening angle of the jet.
2. The rapidity difference between the two gluons should be greater than unity,  $\Delta y_{23} > 1$ . This ensures that the gluons are well separated, and not collinear.

Additionally, there is an ambiguity in which jet to create of the two choices,  $qg$  and  $g\bar{q}$ . For this analysis, the jet was chosen to be the dipole with the smallest rapidity separation  $\Delta y$ , informed by the intuition that the most suitable jets will be formed from collinear colour-partners.

The results from these studies are presented in Fig. 5, where both plots were subjected to the two conditions above. The topologies which violated these conditions performed poorly, as expected, and were thus removed to allow the study of those which were expected to perform well. The requirement  $\Delta y_{23} > 1$  was found to be the smallest rapidity separation which allowed for clear results, while not removing too many samples. The following features are clear in the results.

- The dipole-antenna plot is largely the same as Fig. 3, however the above restrictions exposed a large underestimated region between  $-3 < \ln p_{12}^2/p_{11}^2 < -1$ . This region is not present within the jet-antenna plot, which instead experienced a general improvement. Below this region, the emissions were soft and thus jet recoil is unnecessary;  $\langle R_4^{\text{jet}} \rangle$  experiences no improvement.
- Interestingly,  $\langle R_4^{\text{dip}} \rangle$  was superior around  $\ln p_{12}^2/p_{11}^2 = -1$ , counter to the intuition regarding commensurate momenta emissions developed in section 3.1. This structure was not present in Fig. 3, when the two conditions above were absent. This suggests those conditions are also beneficial for dipole-antenna kinematics.
- There is a significant underestimated region for large  $p_{11}^2$  in  $\langle R_4^{\text{jet}} \rangle$ . This was likely caused by the absence of necessary finite (non-singular) terms in the antenna functions, and not a result of the kinematics map.

The final point justifies some elaboration. Finite terms were removed from the antenna functions during the initial shower operator construction (Eq. 1.8) to take advantage of the pure singularity structure. Universal finite terms can sometimes be reinstated in antenna functions by considering the spin contributions from massive boson decays [52]. Alternatively matrix-element corrections can be performed to restore the finite terms excluded from the antenna functions. We will discuss such corrections in the following section.

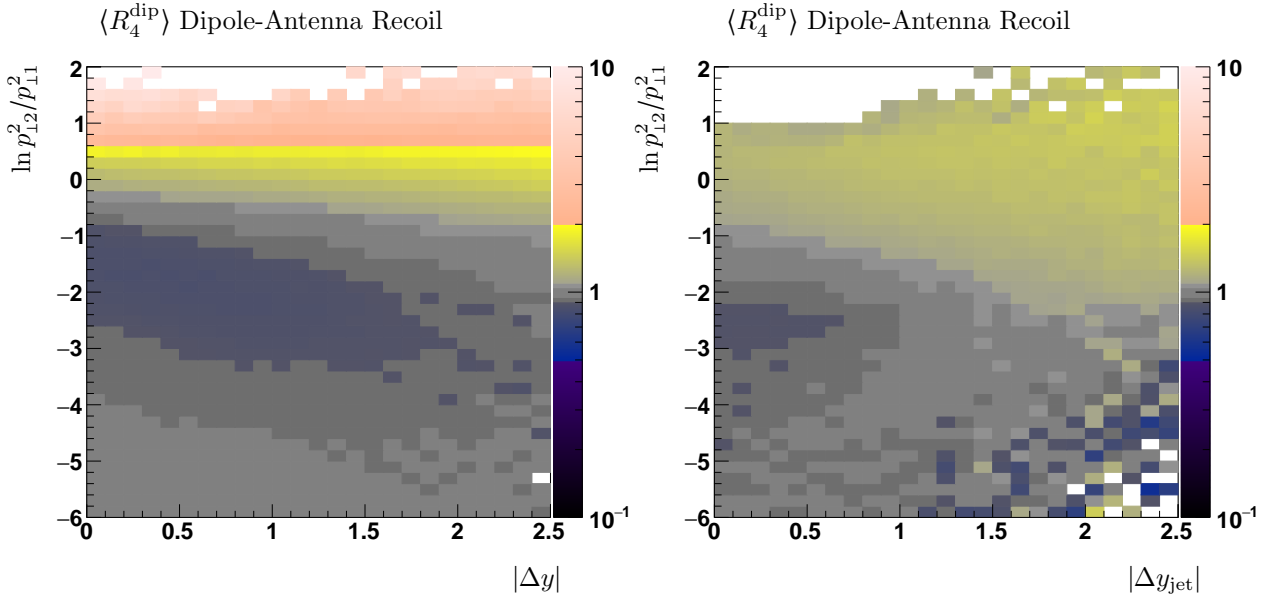


Figure 6: Left:  $\langle R_4^{\text{dip}} \rangle$  across phase space parameterised by the rapidity difference and the hardness of  $g_2$  with respect to  $g_1$ .  $\Delta y$  is defined as the by the same partons which form  $\Delta y_{\text{jet}}$  in Right. Colour lines are not crossed in these samples, and both gluons must be separated by at least one unit of rapidity. Right:  $\langle R_4^{\text{jet}} \rangle$  for the same configuration as left.  $\Delta y_{\text{jet}}$  is defined as the smallest quark-gluon rapidity separation in the event.

As jet recoils were expected to be dependent on rapidity configurations, it was also prudent to consider these results with respect to the rapidity difference  $\Delta y_{\text{jet}}$  of the two partons forming the jet. These results are presented in Fig. 6, where the horizontal axis was replaced due to the approximate independence of the results on  $p_{11}^2$ . The following features are clear.

- Broadly speaking, the size of the central underestimated region was reduced when jet kinematics were employed. It remains unclear if the remaining under-counting region is due to finite terms missing from the antenna function, or some other feature obscured in Fig. 5.
- $\langle R_4^{\text{jet}} \rangle$  approached unity around  $\ln p_{12}^2/p_{11}^2 \sim 1.5$  for small rapidity separations but worsened as  $\Delta y$  increased. Jet recoils performed better at intermediate rapidity separations. However if the aforementioned underestimated region for small  $\Delta y_{\text{jet}}$  is due to missing finite terms, then this conclusion is marred.

#### 4.4 Consensus and Future Extensions

As expected, we found that some regions of phase space are improved by jet-antenna kinematics, while others are not. However, we must be careful in making broad conclusions about the success or failure of these studies, since they are highly dependent on the configurations chosen. It is likely that not all the scenarios which benefit from jet kinematics have been analysed.

Ideally one would develop a simple set of ‘jet criteria’ which would classify emissions as suitable or unsuitable for jet-antenna kinematics. Enforcing that emissions be colour-ordered and that  $\Delta y_{23} > 1$  is one such simple set of criteria, however this also appeared to benefit dipole-antenna kinematics to some extent. Therefore, there are several desirable extensions

to the studies presented above which were beyond the scope of this project, and are necessary to establish such criteria. The following questions remain to be investigated.

- What other jet recoil parameters can be varied to further test the behaviour? Jet-antenna kinematics are highly dependant on the topology of the event, and not all configurations were studied explicitly. A machine-learning survey of the full parameter space could be employed to optimise  $\langle R_4^{\text{jet}} \rangle$  across phase space. This may provide a more empirical set of jet-recoil criteria than those found by manual observation.
- Can matrix-element corrections be employed to introduce any finite-terms potentially required for the jet antenna-functions? Such terms may improve the results presented in the above studies, removing the underestimated regions. However, if such terms are required it could complicate the implementation of the jet-antenna functions to the extent the jet recoil method becomes undesirable from an efficiency standpoint.
- Is the formation of the jet from the simple addition of four-momenta sufficient, and what other descriptions are suitable? The simple summation presents an a-priori momentum conserving map, with the benefit that the resulting pseudo-mass is simple to interpret. Clustering maps such as  $2 \rightarrow 1$  or  $n \rightarrow 1$  could also be used to generate jets with rapidity and  $p_1^2$  accounted for. However, this would present a significant computational overhead, and the results from this work do not indicate how or if this would lead to improvement.

Furthermore, for real parton shower applications, jet-antenna kinematics would need to be generalised beyond the simple four-parton events used in this initial study. Such generalisations dramatically increase the number of possible jet combinations. Five-parton topologies may contain two jets, or one jet containing three partons, and so forth. New studies would need to be performed to test these cases.

In order to consider jet kinematics in the context of arbitrary parton showers, a definitive jet criterion would need to be established. Once in hand however, there is little reason to suspect jet kinematics would not generalise to larger multiplicities. Parton showers will tend to form jets (in the traditional sense) due to the enhancement associated with collinear radiation. These jets are physical structures consisting of collimated partons, which may be measured experimentally using event-shape observables such as thrust or jet-broadening. In these scenarios jet kinematics treat each traditional jet as a single pseudo-parton, with a single net colour. The jet is allowed to recoil as a single body, distributing the total recoil amongst the constituent partons.

Furthermore, the approximate scale invariance of QCD implies that jet-antenna kinematics should be valid at all orders of the parton-shower evolution. This includes within the substructure of traditional jets, as well as for wide angle emission between jets. In these situations the recoil may be negligible within the whole event, but significant in the local vicinity of the dipole, and thus should be accounted for.

Finally there is the ultimate goal of achieving NLL accuracy for the Vincia shower. As discussed in section 3.1 there are NLL effects associated with hard, wide-angle emissions, which jet-antenna kinematics were theorised to improve. It is clear that the initial implementation still exhibits the subleading effects associated with commensurate momenta emissions  $x_{11} \sim x_{12}$ . In fact the improvement observed for jet recoils appears around  $\ln p_{12}^2/p_{11}^2 \sim -2$ . Therefore, we cannot conclude that jet-antenna kinematics will correspond to an improvement in the logarithmic accuracy of Vincia.

In order to suggest such an improvement, the logarithmic accuracy of Vincia would need

to be ascertained using the methods outlined in section 3.2. If the technical challenges surrounding these studies can be overcome, the dipole and jet-antenna kinematics maps may be compared with analytically resummed results. If jet recoil corresponds to an improvement in the logarithmic accuracy of shower results, then they can potentially contribute to the NLL-compatibility of Vincia. It is not expected that jet-antenna kinematics can solely achieve NLL-accuracy.

## 5 Conclusions

In this thesis we presented a complete construction of a basic parton-shower event generator for timelike gluon emission using the Vincia dipole-antenna formalism. The generation of logarithmic structures from the antenna-functions was used to emphasise the empirical shortcomings observed for hard, wide-angle emissions. A novel jet-antenna kinematics map was subsequently developed to address this problem by reducing the excessive transverse recoil assigned to the dipole parents. This was intended to mimic the capability of global recoil schemes which do not tend to suffer from these deficiencies. This jet recoil scheme was not intended to improve all events, and was expected to fail in regions where jets could not be clearly defined. Numerical studies were conducted to establish the criteria with which jet recoils should be utilised. Improvements were observed in several regions of the phase space, but not necessarily where expected. Furthermore, it was challenging to isolate these regions of improvement using the typical phase space variables, making it difficult to establish jet-recoil criteria. Nevertheless, it is clear that jet-antenna kinematics do offer an improvement in many instances, and should readily generalise to more complicated multiplicities provided criteria for their use can be established. Several avenues for further investigation were highlighted, with the hope that ongoing investigations regarding the logarithmic accuracy of Vincia can be incorporated and used to assess the performance of the jet-antenna kinematics map more directly.

## References

- [1] CERN Yellow Reports: Monographs, *Cern yellow reports: monographs, vol. 1 (2022): european strategy for particle physics - accelerator research and development roadmap*, 2022.
- [2] A. Buckley, J. Butterworth, S. Gieseke, D. Grellscheid, S. Höche, H. Hoeth, F. Krauss, L. Lönnblad, E. Nurse, P. Richardson, S. Schumann, M. H. Seymour, T. Sjöstrand, P. Skands, and B. Webber, “General-purpose event generators for lhc physics”, *Physics reports* **504**, 145–233 (2011).
- [3] P. D. G. et al., “Review of Particle Physics”, *Progress of Theoretical and Experimental Physics* **2022**, 083C01, 10.1093/ptep/ptac097 (2022).
- [4] R. Field and R. Feynman, “A parametrization of the properties of quark jets”, *Nuclear Physics B* **136**, 1–76 (1978).
- [5] B. Andersson, G. Gustafson, L. Lönnblad, and U. Petterson, “Coherence Effects in Deep Inelastic Scattering”, *Z. Phys. C* **43**, 625 (1989).
- [6] C. Bierlich, S. Chakraborty, N. Desai, L. Gellersen, I. Helenius, P. Ilten, L. Lönnblad, S. Mrenna, S. Prestel, C. T. Preuss, T. Sjöstrand, P. Skands, M. Uthmeim, and R. Verheyen, “A comprehensive guide to the physics and usage of pythia 8.3”, 2203.11601 (2022).

- [7] J. Bellm, G. Bewick, S. F. Ravasio, S. Gieseke, D. Grellscheid, P. Kirchga er, F. Loshaj, M. R. Masouminia, G. Nail, A. Papaefstathiou, S. Pl tzer, R. Podskubka, M. Rauch, C. Reuschle, P. Richardson, P. Schichtel, M. H. Seymour, A. Si dmok, and S. Webster, “Herwig 7.2 release note”, EPJ **80**, 1912.06509 (2020).
- [8] E. Bothmann, G. S. Chahal, S. H che, J. Krause, F. Krauss, S. Kuttimalai, S. Liebschner, D. Napoletano, M. Sch nherr, H. Schulz, S. Schumann, and F. Siegert, “Event generation with sherpa 2.2”, SciPost Physics **7**, 1905.09127 (2019).
- [9] W. T. Giele, D. A. Kosower, and P. Z. Skands, “A simple shower and matching algorithm”, Physical Review D **78**, 0707.3652 (2008).
- [10] P. Skands, N. Fischer, S. Prestel, and M. Ritzmann, *The vincia antenna shower for hadron colliders*, 2016.
- [11] F. Herren, S. H che, F. Krauss, D. Reichelt, and M. Schoenherr, *A new approach to color-coherent parton evolution*, 2022.
- [12] L. L nnblad, “Ariadne version 4 — a program for simulation of qdc cascades implementing the colour dipole model”, Computer Physics Communications **71**, 15–31 (1992).
- [13] S. H che and S. Prestel, “The midpoint between dipole and parton showers”, EPJ **75**, 1506.05057 (2015).
- [14] M. van Beekveld, S. F. Ravasio, G. P. Salam, A. Soto-Ontoso, G. Soyez, and R. Verheyen, “PanScales parton showers for hadron collisions: formulation and fixed-order studies”, JHEP **2022**, 2205.02237 (2022).
- [15] M. Gell-Mann, “Symmetries of baryons and mesons”, Phys. Rev. **125**, 1067–1084 (1962).
- [16] G. Altarelli and G. Parisi, “Asymptotic Freedom in Parton Language”, Nucl. Phys. B **126**, 298–318 (1977).
- [17] J. C. Collins, A. Duncan, and S. D. Joglekar, “Trace and Dilatation Anomalies in Gauge Theories”, Phys. Rev. D **16**, 438–449 (1977).
- [18] H. D. Politzer, “Reliable Perturbative Results for Strong Interactions?”, Phys. Rev. Lett. **30**, 1346–1349 (1973).
- [19] D. J. Gross and F. Wilczek, “Ultraviolet Behavior of Nonabelian Gauge Theories”, Phys. Rev. Lett. **30**, edited by J. C. Taylor, 1343–1346 (1973).
- [20] M. Schwartz, *Quantum field theory and the standard model*, Quantum Field Theory and the Standard Model (Cambridge University Press, 2014).
- [21] W. T. Giele, D. A. Kosower, and P. Z. Skands, “Higher-order corrections to timelike jets”, Physical Review D **84**, 1102.2126 (2011).
- [22] T. Kinoshita, “Mass singularities of feynman amplitudes”, Journal of Mathematical Physics **3**, 650–677 (1962).
- [23] T. D. Lee and M. Nauenberg, “Degenerate systems and mass singularities”, Phys. Rev. **133**, B1549–B1562 (1964).
- [24] L. L nnblad, “Correcting the colour-dipole cascade model with fixed order matrix elements”, JHEP **2002**, 046–046 (2002).
- [25] S. Catani, F. Krauss, B. R. Webber, and R. Kuhn, “QCD matrix elements + parton showers”, JHEP **2001**, 063–063 (2001).

- [26] A. G.-D. Ridder, M. Ritzmann, and P. Skands, “Timelike dipole-antenna showers with massive fermions”, *Physical Review D* **85**, 1108.6172 (2012).
- [27] V. V. Sudakov, “Vertex parts at very high-energies in quantum electrodynamics”, *Sov. Phys. JETP* **3**, 65–71 (1956).
- [28] A. G.-D. Ridder, T. Gehrmann, and E. Glover, “Antenna subtraction at NNLO”, *Journal of High Energy Physics* **2005**, 056–056 (2005).
- [29] M. Peskin and D. Schroeder, *An introduction to quantum field theory*, Advanced book classics (Avalon Publishing, 1995).
- [30] D. A. Kosower, “Antenna factorization of gauge-theory amplitudes”, *Physical Review D* **57**, 5410–5416 (1998).
- [31] G. Altarelli and G. Parisi, “Asymptotic Freedom in Parton Language”, *Nucl. Phys. B* **126**, 298–318 (1977).
- [32] Y. L. Dokshitzer, “Calculation of the Structure Functions for Deep Inelastic Scattering and  $e^+ e^-$  Annihilation by Perturbation Theory in Quantum Chromodynamics.”, *Sov. Phys. JETP* **46**, 641–653 (1977).
- [33] V. N. Gribov and L. N. Lipatov, “Deep inelastic  $e p$  scattering in perturbation theory”, *Sov. J. Nucl. Phys.* **15**, 438–450 (1972).
- [34] J. J. Lopez-Villarejo and P. Skands, “Efficient matrix-element matching with sector showers”, *JHEP* **2011**, 1109.3608 (2011).
- [35] F. A. Dreyer, G. P. Salam, and G. Soyez, “The lund jet plane”, *JHEP* **2018**, 1807.04758 (2018).
- [36] G. Grunberg, “Renormalization Group Improved Perturbative QCD”, *Phys. Lett. B* **95**, 70 (1980).
- [37] K. Hamilton, R. Medves, G. P. Salam, L. Scyboz, and G. Soyez, “Colour and logarithmic accuracy in final-state parton showers”, *Journal of High Energy Physics* **2021**, 2011.10054 (2021).
- [38] H. Brooks, C. T. Preuss, and P. Skands, “Sector showers for hadron collisions”, *JHEP* **2020**, 2003.00702 (2020).
- [39] E. Boos, M. Dobbs, W. Giele, I. Hinchliffe, J. Huston, V. Ilyin, J. Kanzaki, K. Kato, Y. Kurihara, L. Lonnblad, M. Mangano, S. Mrenna, F. Paige, E. Richter-Was, M. Seymour, T. Sjostrand, B. Webber, and D. Zeppenfeld, *Generic user process interface for event generators*, 2001.
- [40] M. van Beekveld, S. F. Ravasio, G. P. Salam, A. Soto-Ontoso, G. Soyez, and R. Verheyen, “PanScales parton showers for hadron collisions: formulation and fixed-order studies”, *JHEP* **2022**, 2205.02237 (2022).
- [41] J. Alwall, R. Frederix, S. Frixione, V. Hirschi, F. Maltoni, O. Mattelaer, H.-S. Shao, T. Stelzer, P. Torrielli, and M. Zaro, “The automated computation of tree-level and next-to-leading order differential cross sections, and their matching to parton shower simulations”, *JHEP* **2014**, 1405.0301 (2014).
- [42] M. Dasgupta, F. A. Dreyer, K. Hamilton, P. F. Monni, and G. P. Salam, “Logarithmic accuracy of parton showers: a fixed-order study”, *JHEP* **2018**, 1805.09327 (2018).
- [43] G. Luisoni and S. Marzani, “QCD resummation for hadronic final states”, *Journal of Physics G: Nuclear and Particle Physics* **42**, 103101 (2015).

- [44] M. Dasgupta, F. Dreyer, K. Hamilton, P. F. Monni, G. P. Salam, and G. Soyez, “Parton showers beyond leading logarithmic accuracy”, *Physical Review Letters* **125**, 2002. 111114 (2020).
- [45] D. A. Kosower and B. Page, “Universal decomposition of phase-space integrands”, *Physical Review D* **107**, 2211.14156 (2023).
- [46] G. ’t Hooft, “A Planar Diagram Theory for Strong Interactions”, *Nucl. Phys. B* **72**, edited by J. C. Taylor, 461 (1974).
- [47] Z. Nagy and D. E. Soper, “Parton showers with quantum interference”, *Journal of High Energy Physics* **2007**, 114–114 (2007).
- [48] Z. Nagy and D. E. Soper, “Effects of subleading color in a parton shower”, *JHEP* **07**, 119 (2015).
- [49] Z. Nagy and D. E. Soper, “Parton showers with more exact color evolution”, *Phys. Rev. D* **99**, 054009 (2019).
- [50] R. Kleiss, W. J. Stirling, and S. D. Ellis, “A New Monte Carlo Treatment of Multiparticle Phase Space at High-energies”, *Comput. Phys. Commun.* **40**, 359 (1986).
- [51] R. Kleiss, “Phase Space Monte Carlo”, *NATO Sci. Ser. C* **554**, edited by W. Kittel, P. Mulders, and O. Scholten, 281–294 (2000).
- [52] A. J. Larkoski and M. E. Peskin, “Antenna splitting functions for massive particles”, *Physical Review D* **84**, 1106.2182 (2011).